The Local Cluster Survey. I. Evidence of Outside-in Quenching in Dense Environments

Rose A. Finn[1] , Vandana Desai[2] , Gregory Rudnick[3] , Michael Balogh[4], Martha P. Haynes[5] , Pascale Jablonka[6],
Rebecca A. Koopmann[7], John Moustakas[1], Chien Y. Peng[8], Bianca Poggianti[9] , Kenneth Rines[10], and Dennis Zaritsky[11]

[1] Department of Physics & Astronomy, Siena College, 515 Loudon Road, Loudonville, NY 12211, USA; rfinn@siena.edu
[2] IPAC, Mail Code 100-22, Caltech, 1200 E. California Boulevard, Pasadena, CA, 91125, USA
[3] University of Kansas, Department of Physics and Astronomy, Malott Hall, Room 1082, 1251 Wescoe Hall Drive, Lawrence, KS 66045, USA
[4] Department of Physics and Astronomy, University of Waterloo, 200 University Avenue West, Waterloo, Ontario, Canada N2L 3G1, CAN
[5] Cornell Center for Astrophysics and Planetary Science, 530 Space Sciences Building, 122 Sciences Drive, Ithaca, NY 14853, USA
[6] Observatoire de l'Université de Genève, Laboratoire d'Astrophysique de l'Ecole Polytechnique Fédérale de Lausanne (EPFL), 1290 Sauverny, Switzerland
[7] Department of Physics & Astronomy, Union College, Schenectady, NY, 12308, USA
[8] Giant Magellan Telescope Observatory, 465 N. Halstead Street, Suite 250, Pasadena, CA 91107, USA
[9] Osservatorio Astronomico, vicolo dell'Osservatorio 5, 35122 Padova, Italy
[10] Department of Physics & Astronomy, Western Washington University, Bellingham, WA 98225, USA
[11] Steward Observatory, 933 N. Cherry Avenue, University of Arizona, Tucson, AZ 85721, USA
Received 2017 January 11; revised 2018 May 2; accepted 2018 May 6; published 2018 August 1

Abstract

The goal of the *Local Cluster Survey* is to look for evidence of environmentally driven quenching among star-forming galaxies in nearby galaxy groups and clusters. Quenching is linked with environment and stellar mass, and much of the current observational evidence comes from the integrated properties of galaxies. However, the relative size of the stellar and star-forming disk is sensitive to environmental processing and can help identify the mechanisms that lead to a large fraction of quenched galaxies in dense environments. Toward this end, we measure the size of the star-forming disks for 224 galaxies in nine groups and clusters ($0.02 < z < 0.04$; SFR $> 0.1\,M_\odot\,\mathrm{yr}^{-1}$) using 24 μm imaging from the *Spitzer Space Telescope*. We normalize the 24 μm effective radius (R_{24}) by the size of the stellar disk (R_d). We find that star-forming galaxies with higher bulge-to-total ratios (B/T) and galaxies in more dense environments have more centrally concentrated star formation. Comparison with H I mass fractions and NUV $- r$ colors indicates that a galaxy's transition from gas-rich and blue to depleted and red is accompanied by an increase in the central concentration of star formation. We build a simple model to constrain the timescale over which the star-forming disks shrink in the cluster environment. Our results are consistent with a long-timescale (>2 Gyr) mechanism that produces outside-in quenching, such as the removal of the extended gas halo or weak stripping of the cold disk gas.

Key words: galaxies: clusters: general – galaxies: evolution – galaxies: groups: general – galaxies: star formation

1. Introduction

Galaxy clusters host a smaller fraction of actively star-forming galaxies than the general field (e.g., Balogh et al. 1997; Poggianti et al. 1999; Lewis et al. 2002; Gómez et al. 2003; Finn et al. 2005, 2008, 2010; Postman et al. 2005). Even at fixed stellar mass, the fraction of star-forming galaxies tends to decrease with increasing environmental density (e.g., Peng et al. 2010). The mass accretion rate of clusters (e.g., McGee et al. 2009), combined with the assumption that all accreted galaxies eventually quench their star formation, implies that quenching must take place over a long timescale, 3–7 Gyr (e.g., Balogh et al. 2000; Ellingson et al. 2001; Kimm et al. 2009; Peng et al. 2010; De Lucia et al. 2012; Wetzel et al. 2012).

However, trying to uncover the physics that drives this transformation by studying the properties of galaxies during the transition has proved difficult and controversial. A small fraction of galaxies are found in a post-starburst phase, which implies a rapid truncation timescale (Dressler & Gunn 1983); this fraction may depend on environment and redshift (e.g., Zabludoff et al. 1996; Balogh et al. 1999; Poggianti et al. 1999; Tran et al. 2007; Mok et al. 2013; Muzzin et al. 2013). However, the bulk of the star-forming population in clusters looks very similar to those in the field, in terms of their star formation rate and color distribution (Balogh et al. 2004; Baldry et al. 2006; McGee et al. 2011), with just the relative fraction of star-forming and quiescent galaxies varying with environment. Few galaxies, at least at low redshift, seem to inhabit the green valley region that separates star-forming from quiescent galaxies, which implies that the transition itself must happen rapidly, on timescales <1 Gyr (Wetzel et al. 2012).

To reconcile these facts, Wetzel et al. (2012, 2013) proposed a two-stage model in which star formation truncation happens rapidly, but only after a lengthy delay time following accretion into a cluster or group. In the model as originally proposed, galaxies experience little or no change in their star formation rates during the delay phase. Understanding how galaxies could remain uninfluenced by their environment for so long has been a theoretical challenge. Nonetheless, the model has been used successfully to interpret a range of observations at redshifts out to $z = 1$ (van der Burg et al. 2013; Mok et al. 2014; Muzzin et al. 2014; Haines et al. 2015; Knobel et al. 2015; Fossati et al. 2017). Following the delay, the process of galaxy quenching proceeds on a rapid timescale of <1 Gyr.

Despite the success of this delay+rapid quenching model, the hypothesis that galaxies are completely unaffected during the delay period remains controversial. Several studies have shown evidence that at a fixed stellar mass, star formation rates of galaxies in dense environments are skewed to lower values than in the general field (e.g., Koopmann & Kenney 2004a; Poggianti et al. 2008; Gallazzi et al. 2009; Wolf et al. 2009; Finn et al. 2010; Vulcani et al. 2010; Haines et al. 2013; Lin et al. 2014; Taranu et al. 2014; Rodríguez del Pino et al. 2017).

This would imply that there *are* environmental processes at work during the several Gyrs after infall. The delay period might then simply be a time during which long-timescale processes are slowly altering the cluster galaxies, prior to the ultimate termination of star formation in a rapid quenching phase (e.g., Haines et al. 2015).

In this paper, we investigate what is happening to galaxies during the delay phase, and we identify delay-phase galaxies as those that have been accreted by a cluster but are still forming stars. Our goal is to measure the relative extent of the gas and stellar disks, because this is a sensitive probe of environmental processing (e.g., Moss & Whittle 2000; Dale et al. 2001; Koopmann et al. 2006; Bamford et al. 2007; Kawata & Mulchaey 2008; Jaffé et al. 2011; Bösch et al. 2013; Bekki 2014; Schaefer et al. 2017). We present a sample of 224 galaxies in 9 low-redshift galaxy groups and clusters, and we map galaxies from the cluster core to the surrounding infall regions. Our galaxy sample spans a large range in stellar mass, which is necessary to help control for any intrinsic quenching mechanisms that may occur independently of environment (e.g., Peng et al. 2010). We use 24 μm imaging from the MIPS camera on *Spitzer Space Telescope* to measure the size of the star-forming disks, and SDSS *r*-band imaging to quantify the size of the stellar disk.

Multiple wavelengths can be used to trace the star-forming regions in galaxies, including UV, Hα, and infrared emission. While 24 μm is a reliable star formation indicator that closely traces Paschen alpha (e.g., Calzetti et al. 2007), different wavelength indicators can vary with dust and metallicity, and may therefore result in different measurements of the spatial extent of the gas disk. Furthermore, different components of the ISM will respond differently to environmental processing (e.g., Boselli et al. 2014). To mitigate systematics associated with our choice of wavelength, we normalize the size of the star-forming disk by the size of the stellar disk. Our conclusions are based upon *differences* in this ratio with environment and intrinsic galaxy properties, rather than absolute measurements.

This paper is organized as follows. We describe the survey and cluster properties in Section 2. In Section 3 we describe the *Spitzer* observations, and in Section 4 we detail the selection and properties of the galaxies in our sample. In Section 5, we present our methods for quantifying the environment of galaxies, and we discuss our measurements of 24 μm sizes in Section 6. Finally, we present our results in Section 7, which show that the properties of star-forming galaxies are altered during the delay, prior to their final quenching. When calculating distance-dependent quantities, we use $H_0 = 70$ km s^{-1}, $\Omega_\Lambda = 0.7$, and $\Omega_M = 0.3$. Stellar masses are calculated as described in Moustakas et al. (2013) and assume a Chabrier initial mass function (Chabrier 2003).

2. The Local Cluster Survey

The nine clusters that compose the *Local Cluster Survey* are listed in Table 1. The sample consists of clusters that have wide-area *Spitzer* MIPS 24 μm mapping and that lie in the SDSS (York et al. 2000) and ALFALFA (Giovanelli et al. 2005) surveys. The clusters are near enough so that a typical spiral can be resolved in a *Spitzer* 24 μm image yet far enough so that the SDSS photometry is reliable ($0.0137 < z < 0.0433$). The clusters purposely span a range of richness, X-ray luminosity, and X-ray temperature so that we can probe the full range of intra-cluster medium properties. In Figure 1, we show X-ray luminosity in the 0.1–2.4 keV band versus
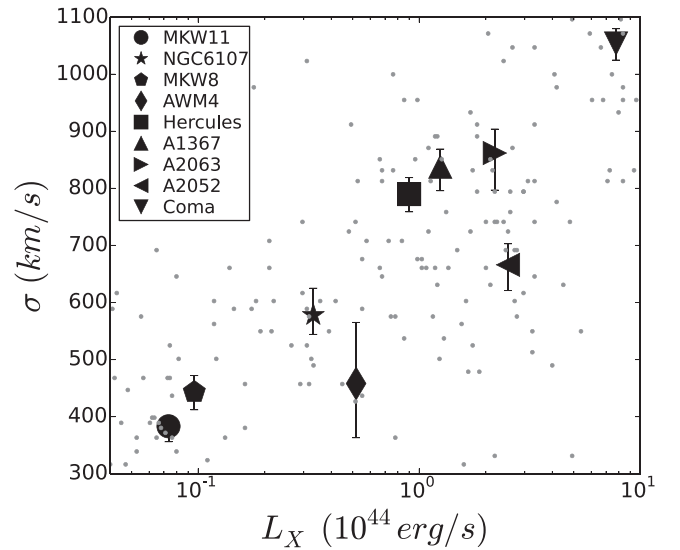
Figure 1. Cluster biweight scale versus X-ray luminosity for Local Cluster Survey sample (large points). The cluster sample purposely spans a large range in X-ray luminosity so that we sample the full range of galaxy environments. The small points show a larger sample of clusters from Mahdavi and Geller (2001) to illustrate that the scatter seen among *Local Cluster Survey* clusters is consistent with the scatter seen among a larger population of clusters.

Table 1
Cluster Properties and Galaxy Sample Sizes

Cluster	Biweight Central Velocity (km s^{-1})	Biweight Scale (km s^{-1})	$N_{\rm gal}$ Core	$N_{\rm gal}$ External
A1367	6505^{+55}_{-54}	838^{+31}_{-42}	6	5
MKW11	6904^{+38}_{-49}	383^{+19}_{-27}	5	13
Coma	7011^{+45}_{-44}	1054^{+26}_{-29}	28	11
MKW8	8039^{+40}_{-38}	443^{+29}_{-31}	0	11
NGC6107	9397^{+57}_{-53}	578^{+47}_{-34}	6	17
AWM4	9604^{+61}_{-55}	458^{+107}_{-95}	4	17
A2063	10410^{+72}_{-74}	862^{+42}_{-65}	27	8
A2052	10431^{+57}_{-64}	666^{+37}_{-45}	7	34
Hercules	10917^{+50}_{-53}	790^{+29}_{-31}	22	3

cluster velocity dispersion for our sample. For comparison, we show a larger sample of clusters from Mahdavi and Geller (2001), with gray points to illustrate that the scatter seen among *Local Cluster Survey* clusters is consistent with the scatter seen among a larger population of clusters.

While Figure 1 demonstrates the range in global cluster environments, the galaxies in our sample also span a wide range of local environments. The galaxies in the MIPS scans of the lower-mass clusters sample both low and high density regions, whereas the galaxies in the MIPS scans of Coma, Hercules, and Abell 1367 provide a more complete sampling of the highest-density environments. An important point to keep in mind as we proceed with the analysis is that Coma galaxies dominate the number counts at high local densities. We investigate how this impacts our results in Section 7.4.

While some clusters have average redshift and velocity dispersions available from the literature, we recalculate the biweight location and scale (Beers et al. 1990) and estimate errors using bootstrap resampling. The galaxies for these calculations and throughout are drawn from the NASA-Sloan Atlas (Blanton et al. 2011), which includes SDSS spectroscopic
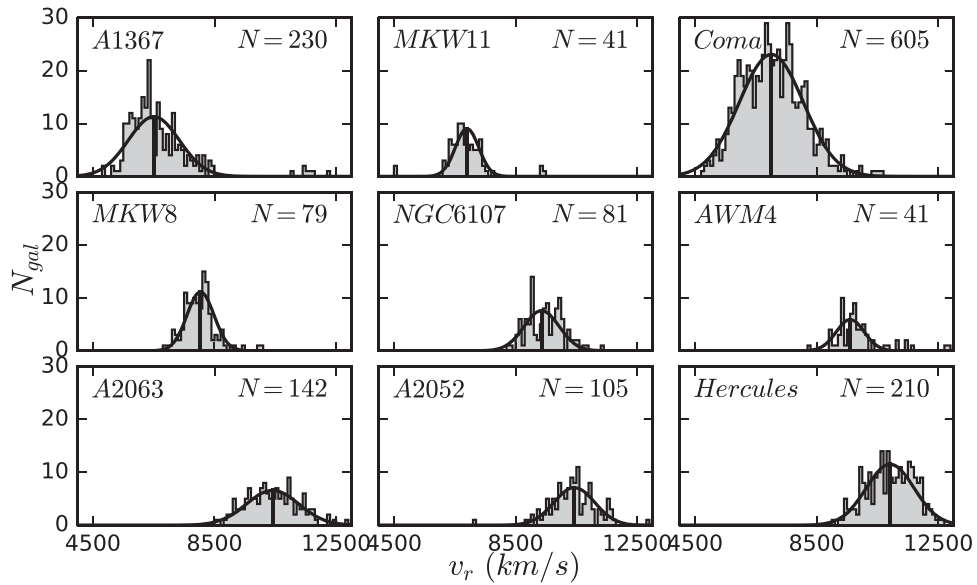
Figure 2. Velocity distribution of NSA galaxies used for the calculation of biweight location and scale. The clusters are ordered by central recession velocity. In each panel, the resulting number of cluster members is indicated in the top right. The vertical black line shows the biweight location, and the black curve shows a Gaussian distribution centered on the biweight location, with a width equal to the biweight scale. N is the number of galaxies with velocity offsets $\Delta v < 3\sigma$ and that have projected radii less that R_{200}.

sources along with other spectroscopically confirmed galaxies from ALFALFA and other surveys. We select all galaxies that have redshifts between $0.0137 < z < 0.0433$, where the lower limit is set by Coma (recession velocity minus $3\sigma_v$) and the upper limit is set by the most distant cluster, Hercules (recession velocity plus 3σ). We first calculate the biweight location and scale using all galaxies, with a recession velocity within 4000 km s^{-1} of each cluster and a projected radius less than 1.7 Mpc (this corresponds to a 1 degree radius at the redshift of Coma). We use this biweight location as the new median and recalculate the location and scale. We repeat this until the scale changes by less than 1 km s^{-1}, which usually happens within two iterations. We use the weighting factors suggested by Beers et al. (1990) to minimize the effect of any galaxy whose velocity deviates by more than $4\sigma_v$ from the central velocity. We show the results in Figure 2 and in Table 1. The errors listed in Table 1 are the 68% confidence interval as determined by bootstrap resampling. In each panel in Figure 2, we list the number of galaxies with velocity offsets $\Delta v < 3\sigma$ that have projected radii less that R_{200}, where R_{200} is calculated from the cluster biweight scale according to the relation in Finn et al. (2008).

3. MIPS Observations and Reduction

Each cluster has 24 μm data from the MIPS instrument (Rieke et al. 2004) on the *Spitzer Space Telescope*, and we use the 24 μm emission to probe the spatial extent of star formation. In Figure 3, we show the positions of galaxies that lie within the 24 μm scan region and have a redshift in the range of $0.0137 < z < 0.0433$. The overall galaxy density is shown with the grayscale, with black and white denoting high and low density areas, respectively. Specifically, white indicates bins with no galaxies, and black indicates regions that contain 10 or more galaxies. The dark gray circles show R_{200}, and the green box shows the footprint of the MIPS scan. With the exception of Coma, A1367, and Hercules, the clusters have
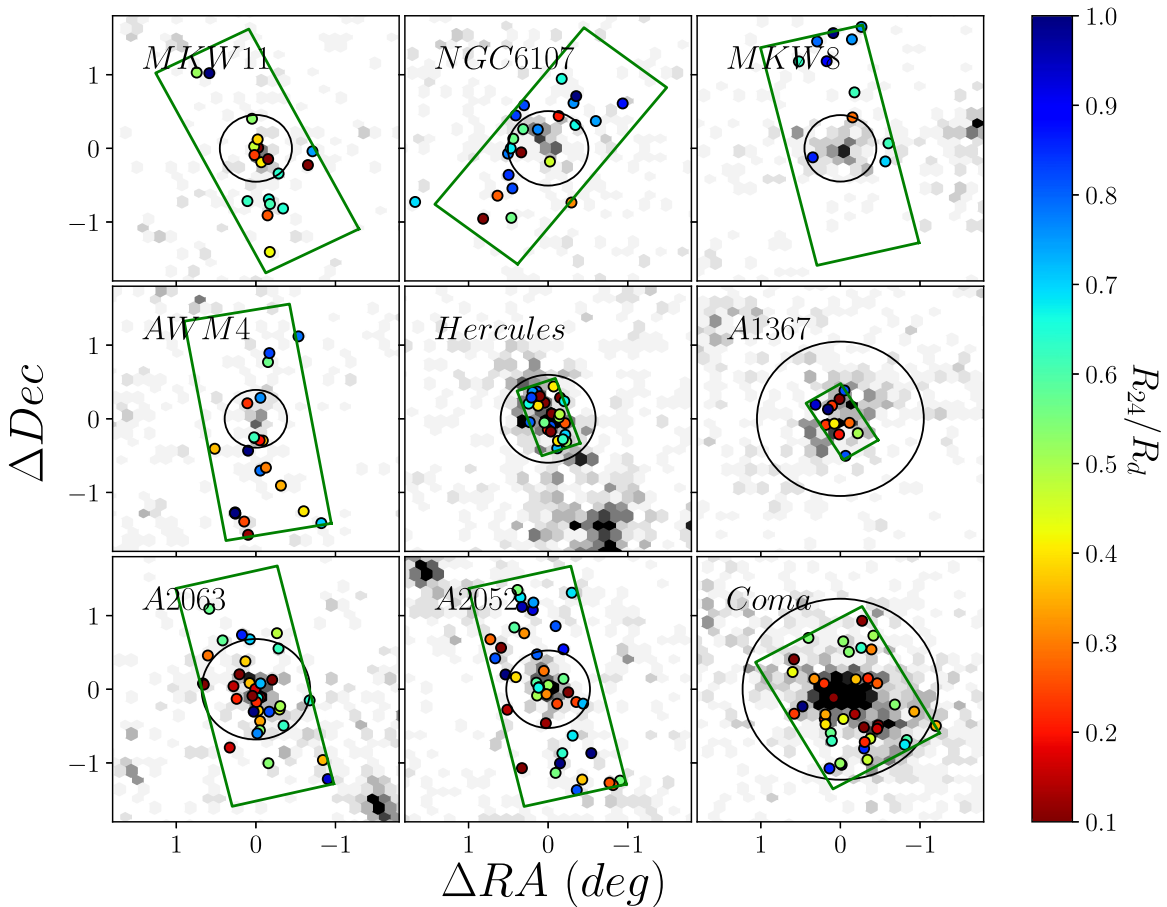
MIPS data obtained specifically for this project, and each scan covers an area of approximately 1.5 × 2.5 square-degree area around each cluster. The MIPS data for Coma, A1367, and Hercules were pulled from the *Spitzer Science Center* archive, and the observations are summarized in Table 2. While the areal coverage for these clusters is smaller, the archive clusters provide an important complement by sampling regions of higher local density and X-ray luminosity (see Figure 1).

The MIPS data are reduced using the MOPEX software package, following the procedure outlined in the *Spitzer* MIPS Data Reduction Cookbook.[12] We use SExtractor (Bertin & Arnouts 1996) to detect galaxies and measure photometry. We measure the noise for each object using the MOPEX-generated standard deviation image. We estimate the depth of each image by placing artificial galaxies on each image and then rerunning SExtractor. We calculate the flux where we recover 80% of the test sources, and we list these flux limits in Table 2. We convert the 80% flux limits to an IR luminosity at the cluster redshift using the templates of Chary and Elbaz (2001) and list these values in the final column of Table 2.

4. Selection of Star-forming Galaxies

Our parent sample consists of exactly 1800 NSA galaxies that lie on the MIPS 24 μm scans and fall in the redshift range $0.0137 < z < 0.0433$. We apply additional selection criteria to ensure that we are sampling the same galaxy population in each cluster. First, to account for the varying sensitivity of the 24 μm scans, we apply a uniform cut in L_{IR} ($L_{IR} > 5.2 \times 10^8 \, L_{\odot}$). This limit is set by the depth of the MIPS scans for Abell 2052 and Abell 2063, which have the highest 80% completeness limit of $L_{IR} = 5.13 \times 10^8 \, L_{\odot}$. Assuming that the 24 μm emission is due to heating from massive stars, this

---

[12] http://irsa.ipac.caltech.edu/data/SPITZER/docs/dataanalysistools/cookbook/home/

Figure 3. Dec versus RA for galaxies in the vicinity of each cluster. Clusters are ordered left-to-right and top-to-bottom by increasing X-ray luminosity. The colored circles show the projected position of galaxies in the GALFIT sample, with the color indicating R_{24}/R_d. The grayscale shows the surface density of galaxies within $\pm 3\sigma_v$, and the large black circles show R_{200}. The green rectangle shows the footprint of the 24 μm MIPS scan.

L_{IR} corresponds to an approximate star formation rate of 0.1 $M_\odot$ yr^{-1}. We retain 541 galaxies after the L_{IR} cut.

We use both optical emission-line ratios and infrared colors to eliminate AGN from our sample. The majority of galaxies in the NASA-Sloan Atlas have optical spectra, and we use the Kauffmann et al. (2003) criteria for separating AGN from star-forming galaxies. For those without optical spectra, we use *WISE* photometry $W1 - W2 > 0.8$ to identify AGN (Stern et al. 2012). (Note that only 10/1800 galaxies in our sample show such red $W1 - W2$ colors. This is likely because this color selects only whopping AGN.) Two galaxies have neither optical spectra nor *WISE* photometry, and so we are not able to classify as AGN versus star-forming; we retain them in the sample nonetheless. After removing AGN, we are left with 351 star-forming galaxies.

We also apply a minimum cut on galaxy size and keep only galaxies with *r*-band effective radii $R_e \geqslant 1.3$ kpc. This corresponds to 1 pixel on the MIPS detector at the distance of our farthest cluster, Hercules ($2''45 = 1.3$ kpc), and we are not confident in measuring sizes that are smaller than a pixel. We retain 332 of the galaxies after applying the size selection.

We attempt to model all of these galaxies using GALFIT (Peng et al. 2002). We remove six galaxies (three pairs) that are close enough to each other to compromise the resulting fits. The modeling fails for another 40 galaxies, and this is usually due to the low signal-to-noise ratio of the 24 μm emission. In

addition, we remove 33 galaxies with observed 24 μm surface brightnesses greater than 20 mag/arcsec^2, because our simulations indicate that the fits are unreliable; we discuss the details of these simulations in the Appendix. We retain 252 galaxies.

Finally, we require galaxies to be in the sample of Simard et al. (2011) because we use their measurements of effective radius and bulge-to-total ratio in our analysis. Simard et al. (2011) perform two-dimensional bulge-to-disk decomposition for more than 1 million galaxies in SDSS DR7 using the GIM2D software. They limit their sample to galaxies with $14 \leqslant m_{\text{petro},r,\text{corr}} \leqslant 18$ and exclude objects that are classified in the DR7 photometry table as saturated or unresolved. We are able to match 89% of our sources to the Simard et al. (2011) catalog, which leaves us with a final sample of 224 galaxies. Of the 28 galaxies not matched to the Simard et al. (2011) catalog, 17 are too bright ($m_r < 14$), 2 are too faint ($m_r > 18$), 2 are blended, 2 are saturated, 1 is not in the DR7 catalog, and 1 seems to have bad coordinates in the DR7 catalog. We are not able to identify the reason why the remaining 3 galaxies are not in the Simard catalog.

5. Quantifying the Environment of Star-forming Galaxies

We will compare the size of the star-forming disk versus environment throughout this paper, and we define environment in two different but related ways. First, we make a simple division in phase space to split the sample into two groups,

Table 2
Spitzer MIPS Observations

Cluster	z	Date of Obs	Program ID	PI	f_{80} (MJy/sr)	$\log_{10}(L_{80}/L_\odot)$
A1367	0.0217	2006 Jun 07	25	Fazio	3.50 ± 0.25	8.25
MKW11	0.0230	2008 Jul 31	50456	Finn	4.00 ± 0.25	8.38
Coma	0.0234	2004 Jun 22	83	Rieke, G.	2.25 ± 0.25	8.12
MKW8	0.0268	2009 Mar 24	50456	Finn	3.75 ± 0.25	8.45
NGC6107	0.0313	2008 May 16	50456	Finn	3.25 ± 0.25	8.50
AWM4	0.0320	2008 Sep 26	50456	Finn	3.50 ± 0.25	8.56
		2008 Sep 28				
A2063	0.0347	2009 Mar 23	50456	Finn	4.00 ± 0.25	8.71
A2052	0.0348	2009 Mar 24	50456	Finn	4.00 ± 0.25	8.71
Hercules	0.0364	2006 Jun 22	25	Fazio	3.25 ± 0.25	8.68

galaxies in the cluster core versus galaxies external to the core. We adopt the cut used by Oman et al. (2013), $|\Delta v/\sigma| < -4/3 \Delta R/R_{200} + 2$, and we show this cut with the black line in Figure 4. This figure includes galaxies from all clusters, and the black shading shows the phase-space positions of all galaxies. The colored points show the GALFIT sample (Section 6). The region in phase space to the left of the black line contains galaxies that are likely to be true cluster members, whereas the region to the right of this line contains galaxies near the cluster as well as a large fraction (>50%) of interlopers that are not physically associated with the cluster (Oman & Hudson 2016). We denote the sample to the left and right of this line as core and external galaxies, respectively. According to this definition, our sample contains 105 core galaxies and 119 external galaxies, and the breakdown of galaxies by cluster is shown in columns 4 and 5 of Table 1.

We note that neither the core nor external samples are pure. The core sample is dominated by galaxies that have been in the cluster environment the longest (e.g., Oman et al. 2013) but may still contain galaxies that are physically distant from the cluster center but lie along the line of sight. In addition, the external sample will contain galaxies in the field as well as backsplash galaxies that have already passed through the cluster core (e.g., Balogh et al. 2000; Bahé et al. 2013). Therefore core/external do not translate cleanly into cluster/field, and this cross-contamination will dilute the observational signatures of any environmental processing.

To demonstrate the similarity and therefore comparability of the core and external subsamples, we show the cumulative distributions for stellar mass, bulge-to-total ratio, redshift, and r-band effective radius in Figure 5. The properties of the core and external galaxies are not statistically different according to both the K-S and Anderson-Darling tests, except with regard to redshift. Coma contributes significantly to the core sample, whereas the redshift distribution of the external sample is skewed slightly toward higher redshift. This difference does not impact our results.

We use local galaxy density as a second metric of galaxy environment. Specifically, we use Σ_5, which is the surface density of galaxies out to the fifth nearest neighbor. When counting neighbors, we use only galaxies in the SDSS spectroscopic sample with $M_r < -18.2$. The magnitude cut corresponds to the SDSS spectroscopic completeness limit ($r < 17.7$) at the distance of our farthest cluster. In addition, we require that neighbors must have a velocity offset $\Delta v < 2500$ km s^{-1}. We note that our two measures of environment are closely related; Σ_5 is strongly correlated with
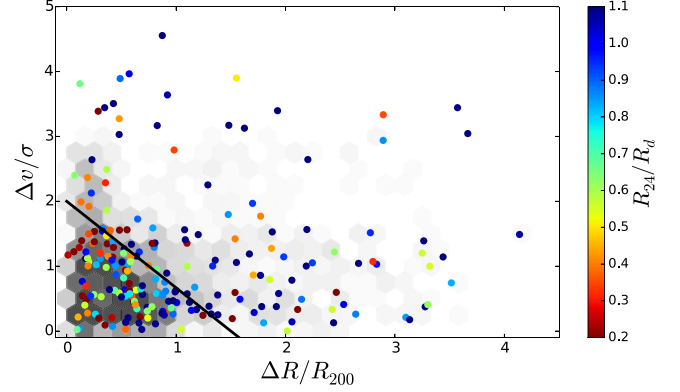
Figure 4. $\Delta v/\sigma$ versus $\Delta R/R_{200}$ for galaxies in the MIPS scans. The colored points show the GALFIT galaxy sample, and the color indicates the relative size of the 24 μm and r-band half-light radii. The grayscale shows the phase-space distribution of both core and external galaxies that lie within the MIPS areal coverage. The black line shows how we separate core and external galaxies (Oman et al. 2013). Seven additional galaxies lie at $\Delta v/\sigma > 5$ but are not shown here, so that galaxies with lower velocity offsets can be seen more clearly. Note that the external sample likely contains galaxies that have already passed through the cluster center.
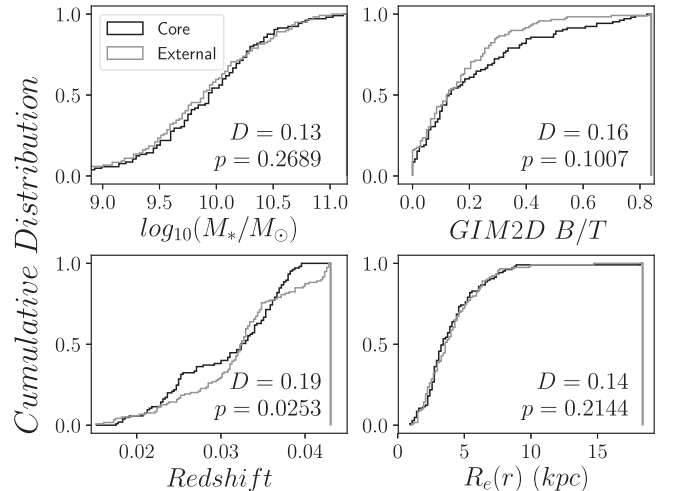
Figure 5. Cumulative distributions of stellar mass, B/T, redshift, and effective radius for core (black) and external galaxies (gray). The K-S D and p-value are shown in each panel. The samples are comparable except in terms of redshift, with the external sample offset to slightly higher values. This difference does not affect our results.

a galaxy's position in phase space. In effect, Σ_5 provides a continuous measure of environmental density as compared to the dichotomous division of core versus external galaxies.

Two clusters in our sample, A2052 and A2063, lie near each other on the plane of the sky and in redshift space, but we are still confident in our ability to quantify the environment of galaxies in this region. The core/external division is preserved around these two structures because while the MIPS scans overlap slightly, there are no galaxies that are classified as external in one field of view and core in another field of view, or vice versa. In addition, the local density metric will account for any enhanced density between the two clusters (see Figure 3).

6. Analysis of Optical and IR Images

Our goal is to measure the size of each galaxy in the optical and infrared to trace the stellar and star-forming components, respectively. Simard et al. (2011) use GIM2D to fit a two-dimensional, single-component *Sérsic* model for a large fraction of DR7 galaxies, and they also fit two versions of bulge+disk models to each galaxy. One version of the bulge +disk models forces the bulge to have an $n = 4$ *Sérsic* profile, and the second set of models allows the *Sérsic* index of the bulge to vary. We use the r-band disk radius (R_d; see Table 3 for a list of definitions of radial size measurements.) for the $n = 4$ bulge+disk models to characterize the size of the stellar disk. We use GALFIT (Peng et al. 2002) to fit a *Sérsic* model to the 24 μm images. To confirm that GALFIT and the GIM2D models are comparable, we fit the r-band images for a subset of the galaxies using GALFIT and find that the GIM2D and GALFIT model parameters are consistent.

6.1. GALFIT Analysis of 24 μm Images

To quantify the 24 μm size of each galaxy, we fit a two-dimensional, single-component *Sérsic* profile to the 24 μm galaxy images using GALFIT (Peng et al. 2002). GALFIT requires a PSF image to properly model galaxies, and this is particularly important when modeling low-resolution data such as the 24 μm scans. We use a point source in each MIPS mosaic as the reference PRF for that field, choosing a bright, isolated source that shows a clear diffraction pattern. For Hercules, we use the PRF provided by *Spitzer Science Center* because our simulations indicate that the PRFs we created were biasing the model parameters (see the Appendix). We make a 30×30 pixel^2 cutout, keeping the star centroid at (16,16) as required by GALFIT. To test the accuracy of the PSF, we select other stars on the image and perform a one-component fit using GALFIT. We are able to model the other point sources well, with little residual remaining after subtracting the model from the image. The model parameters are $R_e \approx 2$ pixels, *Sérsic* index ≈ 1.5, and $B/A = 0.9$–1.0. The fitted magnitudes are comparable to those measured by SExtractor MAG_BEST.

In addition to the PRF image, GALFIT requires an input image, a noise image, and a mask if multiple objects fall within the analysis area. We create cutouts for each galaxy from the MIPS scan, using an analysis area of $100'' \times 100''$ or six times the r-band Petrosian R_{90} (whichever is larger). We mask out other objects in the analysis region using a segmentation image from SExtractor, as suggested in the GALFIT *User Manual*.[13] We review these masks by hand and fix the masks for galaxies that were broken into several objects by SExtractor; this is typically an issue for larger, well-resolved spirals with more
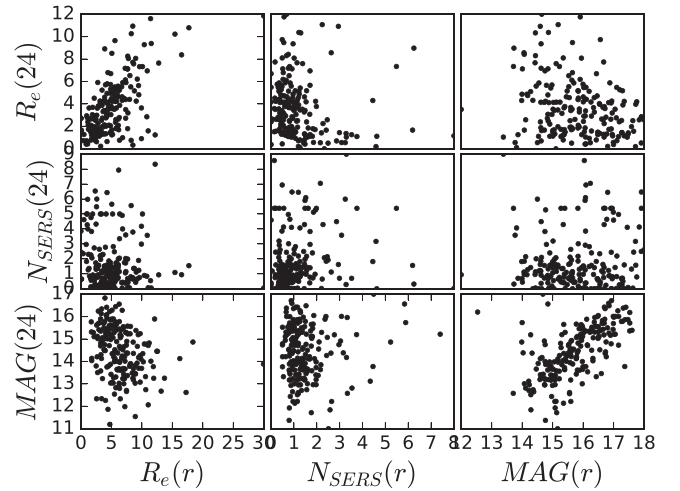
Figure 6. GALFIT 24 μm model parameters versus Simard et al. (2011) r-band model parameters for all galaxies in our final sample. The top-left and bottom-right panels show that 24 μm and r-band effective radius and magnitude are strongly correlated.

clumpy features. We use the standard deviation image that is created by MOPEX as the noise image for GALFIT.

We run GALFIT on each 24 μm image using a one-component *Sérsic* model. We use the GIM2D one-component r-band *Sérsic* model parameters as an initial guess for the 24 μm *Sérsic* fit. Because most galaxies are only marginally resolved at 24 μm, we hold the axis ratio and position angle fixed at the r-band values. If the best-fit *Sérsic* index goes above 6, we refit the galaxy while holding the *Sérsic* index fixed at 5. In some cases, the GALFIT model converges with a numerical error. In most of these cases, the error arises because the 24 μm emission is small and consistent with a point source, and the effective radius of the model galaxy is close to zero. For some of the fainter point-like sources, a model will converge without a numerical error if we let the axis ratio vary. If we are unable to obtain a reliable fit, we remove these galaxies from the sample.

6.2. GALFIT Best-fit Model Parameters

We compare the 24 μm and the r-band *Sérsic* model parameters in Figure 6. The r-band parameters are shown along the horizontal axes, and the GALFIT 24 μm parameters are shown along the vertical axes. The diagonal panels show the corresponding parameters of the r and 24 μm fits. The r and 24 μm effective radii are correlated, as are the model magnitudes. The 24 and r *Sérsic* indices are not strongly correlated, although the bulk of both r and 24 indices are less than 2. This is consistent with a sample dominated by disk galaxies. The top middle panel shows that galaxies with higher r-band *Sérsic* index have systematically lower values of R_{24}, a point we will revisit in Section 7.2. We conclude that there are no strange systematics between the 24 μm and r-band model parameters. We discuss the reliability of the GALFIT model parameters in more detail in the Appendix.

7. Results

7.1. Relative Sizes of the Star-forming and Stellar Disks

We show examples of the 24 μm *Sérsic* models in Figures 7–9. In Figure 7, we show five randomly selected galaxies whose 24 μm emission is more compact than the r-band emission,

---

[13] https://users.obs.carnegiescience.edu/peng/work/galfit/galfit.html
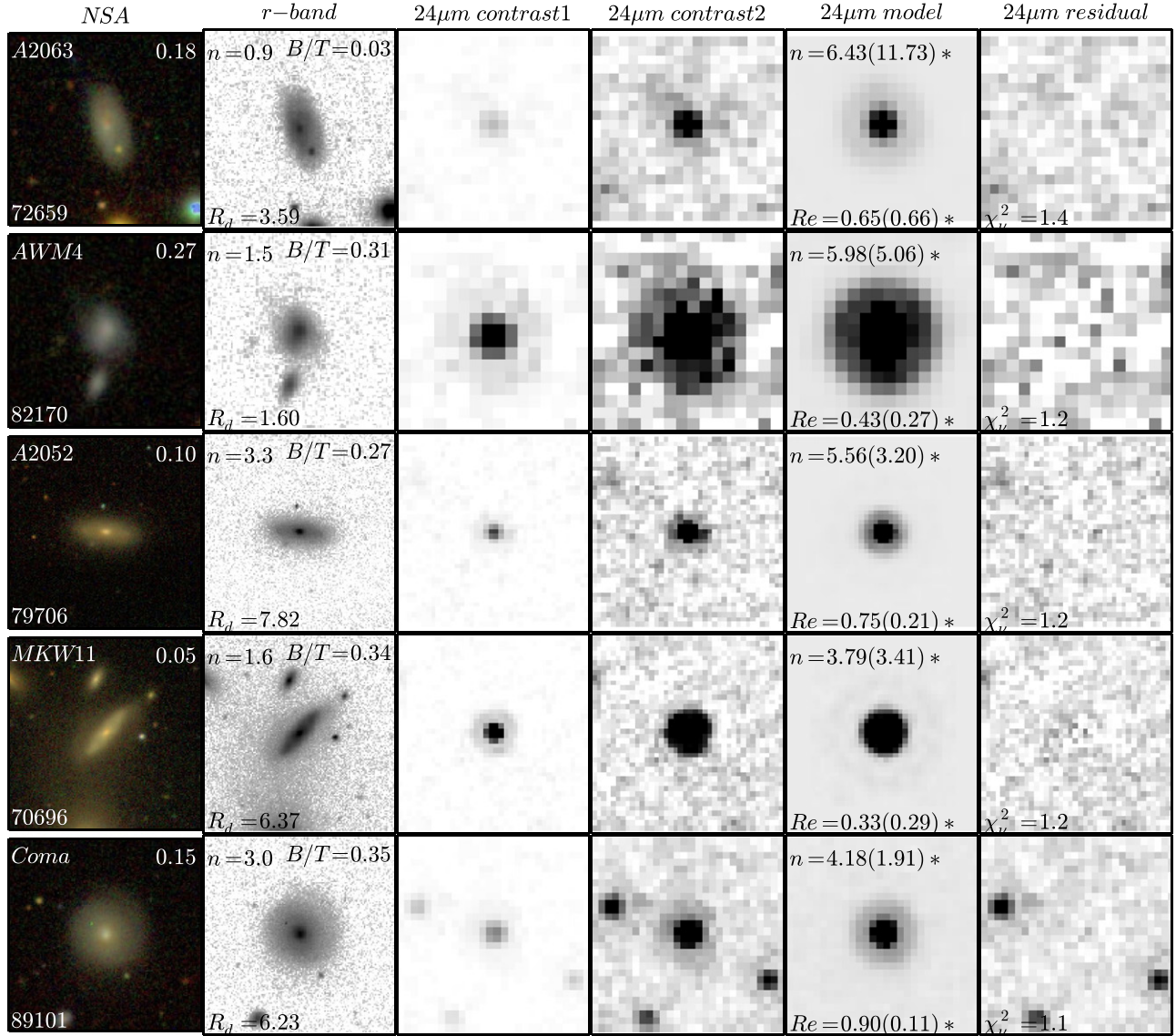
Figure 7. Example GALFIT modeling results for five randomly selected galaxies with R_{24}/R_d between 0 and 0.3. Columns 1 and 2 show the SDSS color and r-band images. Columns 3 and 4 show the 24 μm image at two different stretches to emphasize the high and low surface-brightness features, respectively. Columns 5 and 6 show the 24 μm single-component *Sérsic* model and residual, and the contrast is identical to column 4 to emphasize the low surface-brightness features. The text in column 1 gives the parent cluster, the NSA ID, and R_{24}/R_d. Column 2 lists the r-band *Sérsic* index n, the bulge-to-total ratio, and the disk scale length in arcseconds. The text in column 5 lists the 24 μm *Sérsic* index and effective radius in arcseconds, and column 6 lists χ^2_ν of the best-fit model.

specifically $0.1 < R_{24}/R_d < 0.3$. Columns 1 and 2 show the SDSS color and r-band images, respectively. Columns 3 and 4 show the 24 μm image at two different stretches. The first stretch (*contrast*1) highlights the high surface-brightness features, and the second stretch (*contrast*2) emphasizes the low surface-brightness features. Columns 5 and 6 show the 24 μm *Sérsic* model and residual, and both are shown at *contrast*2. Figure 8 shows five randomly selected galaxies with $0.4 < R_{24}/R_d < 0.7$, and Figure 9 shows five randomly selected galaxies with $R_{24}/R_d > 0.9$. The columns are the same as for Figure 7.

In Figure 10, we plot the effective radius of the best-fit 24 μm model versus the r-band half-light radius for the disk component from Simard et al. (2011) for each cluster pointing. The clusters are ordered left-to-right and top-to-bottom by increasing X-ray luminosity. The solid black line shows a one-to-one correlation. The circles and squares show core and external galaxies, respectively. For all clusters, the 24 μm

and r-band sizes are correlated (see also Figure 6), although the 24 μm half-light radii are systematically smaller than the r-band disk half-light radii R_d.

We show the distribution of R_{24}/R_d for the core and external galaxies in Figure 11. The mean (median) size ratio for the core galaxies is 0.73 (0.69) ± 0.04, where the uncertainty is the error in the mean. The mean (median) size ratio for the external galaxies is 0.91 (0.94) ± 0.04. We use both the K-S and Anderson-Darling tests to compare the distribution of R_{24}/R_d for the core and external galaxies. Both tests reject the null hypothesis at the 3σ level, which indicates that the core galaxies have significantly smaller values of R_{24}/R_d. We therefore find that the spatial distribution of star formation in core galaxies is more concentrated than in external galaxies.

Numerous other studies have measured the relative size of the star-forming and stellar disks as a function of environment at both low (Moss & Whittle 2000; Dale et al. 2001; Koopmann et al. 2006; Schaefer et al. 2017) and intermediate
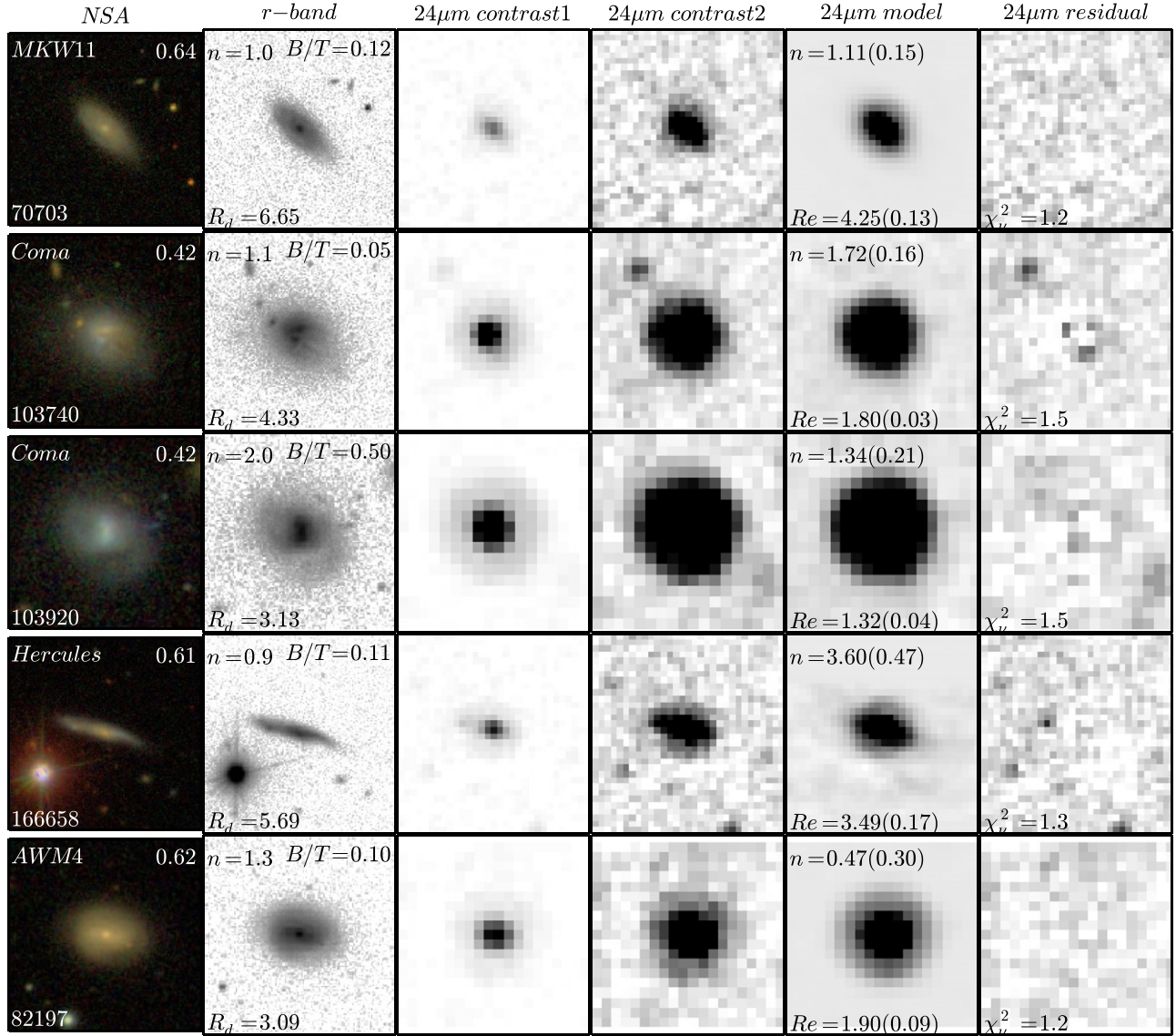
Figure 8. Example GALFIT modeling results for five randomly selected galaxies with R_{24}/R_d between 0.4 and 0.7. Columns 1 and 2 show the SDSS color and r-band images. Columns 3 and 4 show the 24 μm image at two different stretches to emphasize the high and low surface-brightness features, respectively. Columns 5 and 6 show the 24 μm single-component *Sérsic* model and residual, and the contrast is identical to column 4 to emphasize the low surface-brightness features. The text in column 1 gives the parent cluster, the NSA ID, and R_{24}/R_d. Column 2 lists the r-band *Sérsic* index n, the bulge-to-total ratio, and the disk scale length in arcseconds. The text in column 5 lists the 24 μm *Sérsic* index and effective radius in arcseconds, and column 6 lists χ_ν^2 of the best-fit model.

redshift (Bamford et al. 2007; Bösch et al. 2013), and most find that the star-forming region is more concentrated among cluster galaxies than the field. Jaffé et al. (2011) find that the outer extent of the emission-line region is systematically smaller in cluster galaxies.

Our quantitative size estimates of R_{24}/R_d for core (mean, median, error in the mean: 0.73, 0.69, 0.04) and external (mean, median, error in the mean: 0.91, 0.94, 0.04) galaxies are in reasonable agreement with previous work. Koopmann et al. (2006) find $r_{H\alpha}/r_R = 0.91 \pm 0.05$ and 1.18 ± 0.10 for Virgo cluster and field galaxies, respectively (error is error in the mean). At higher redshift, Bösch et al. (2013) find ~ 0.9 and 1.27 for cluster and field galaxies at $z = 0.2$, and Bamford et al. (2007) find $r_{em}/r_B = 0.92 \pm 0.07$ and 1.22 ± 0.06 for $0.2 \lesssim z \lesssim 0.8$ cluster and field galaxies. Jaffé et al. (2011) find a ratio of ~ 0.8 for $0.4 < z < 1$ galaxies that is independent of environment. Interestingly, Jaffé et al. (2011) use the ESO Distant Cluster Survey for their cluster sample,

and these are relatively low-mass clusters. With the exception of Jaffé et al. (2011), our values are systematically lower than most previous measurements that have been made using optical emission lines, but the $\sim 20\%$ offset we find between field and cluster sizes is consistent with previous work.

7.2. R_{24}/R_d versus B/T, Local Galaxy Density, and Stellar Mass

We show how R_{24}/R_d varies with bulge-to-total ratio in the top row of Figure 12. As mentioned in Section 4, the B/T values are from Simard et al. (2011). The sample is divided into full (left), core (middle), and external (right). The points are colored according to stellar mass. The Spearman rank coefficient and probability of the null hypothesis are shown in the top of each panel. To account for the variation in error among the individual 24 μm best-fit models, we create 1000 Monte-Carlo realizations of the data and calculate the

NSA	r−band	24μm contrast1	24μm contrast2	24μm model	24μm residual
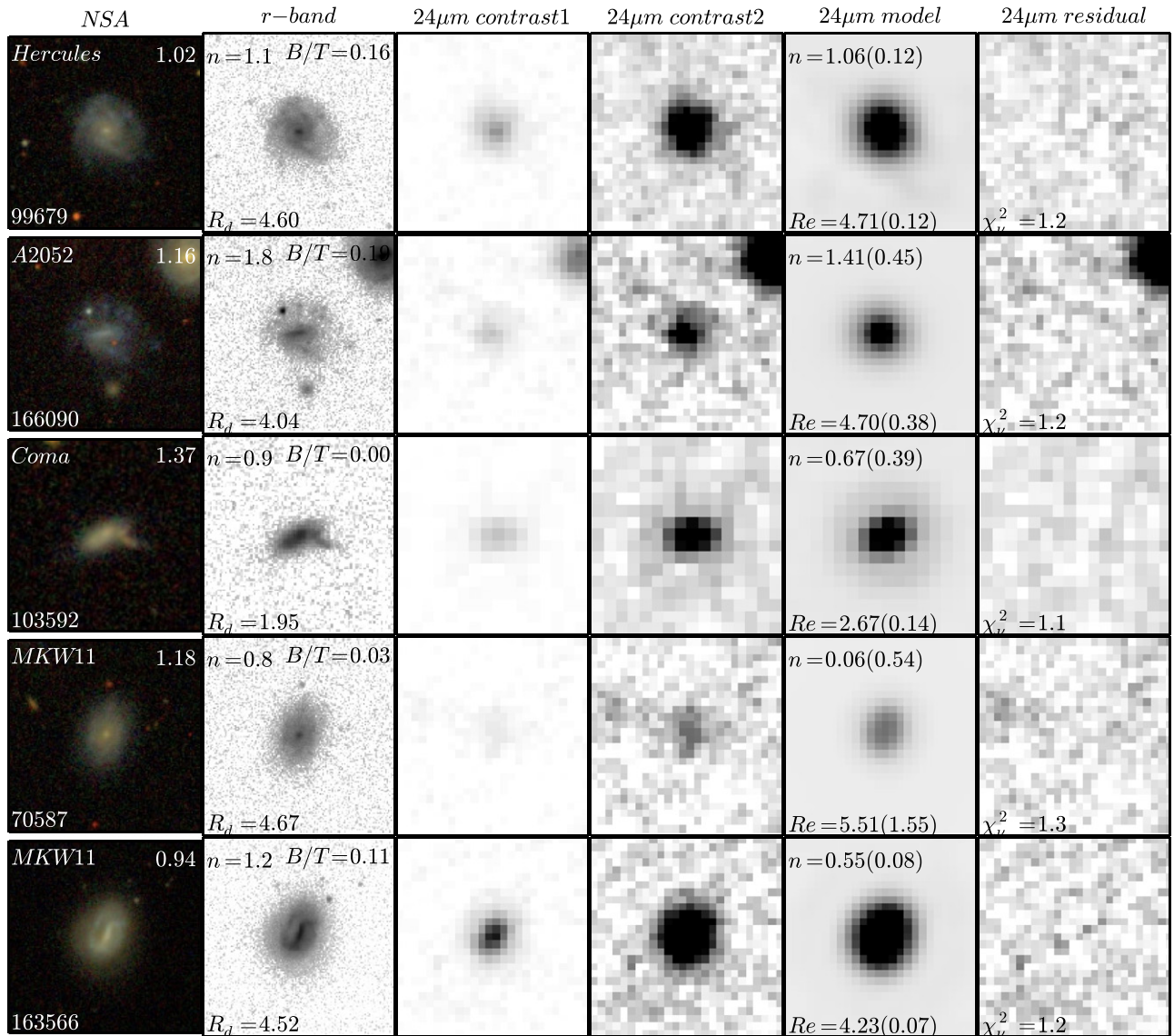
Figure 9. Example GALFIT modeling results for five randomly selected galaxies with R_{24}/R_d greater than 0.9. Columns 1 and 2 show the SDSS color and r-band images. Columns 3 and 4 show the 24 μm image at two different stretches to emphasize the high and low surface-brightness features, respectively. Columns 5 and 6 show the 24 μm single-component *Sérsic* model and residual, and the contrast is identical to column 4 to emphasize the low surface-brightness features. The text in column 1 gives the parent cluster, the NSA ID, and R_{24}/R_d. Column 2 lists the r-band *Sérsic* index n, the bulge-to-total ratio, and the disk scale length in arcseconds. The text in column 5 lists the 24 μm *Sérsic* index and effective radius in arcseconds, and column 6 lists χ^2_ν of the best-fit model.

Spearman rank correlation coefficient for each realization, assuming that the GALFIT errors for R_{24} are normally distributed. We report the 68% confidence interval for the correlation coefficient (ρ) and the probability of no correlation (p). The p-values indicate that R_{24}/R_d and B/T are inversely correlated and that the correlation is strong.

We use bulge-to-total ratio instead of visually classified morphology because Koopmann and Kenney (1998) show that visual classification is biased by the specific star formation rate. More specifically, when comparing galaxies of a fixed concentration, Koopmann and Kenney (1998) show that galaxies with low star formation rates are systematically classified as having an earlier Hubble type.

The *Sérsic* index of a single-component fit can also be used as a proxy for morphology, with the index increasing from 1 to 4 as a galaxy profile goes from disk dominated to bulge dominated. We find a similar correlation between R_{24}/R_d versus the r-band *Sérsic* index, which is not surprising given that B/T and *Sérsic* index are themselves strongly correlated. The result, then, is that galaxies with more concentrated stellar profiles have smaller R_{24}/R_d, and at a given B/T, core galaxies have smaller R_{24}/R_d ratios than the external galaxies.

The correlation between the radial distribution of star formation and morphology has been known for a long time. Mapping the distribution of H II regions in 37 nearby galaxies, Hodge and Kennicutt (1983) find that early-type spirals tend to have centrally concentrated, symmetric star formation, whereas later-type spirals have more extended and asymmetric emission. The results were confirmed by Bendo et al. (2007), who use 24 μm emission to quantify the spatial distribution of star formation for the 65 galaxies in the *Spitzer Infrared Nearby Galaxy Survey*. However, not all previous studies find a link between the spatial distribution of star formation and galaxy
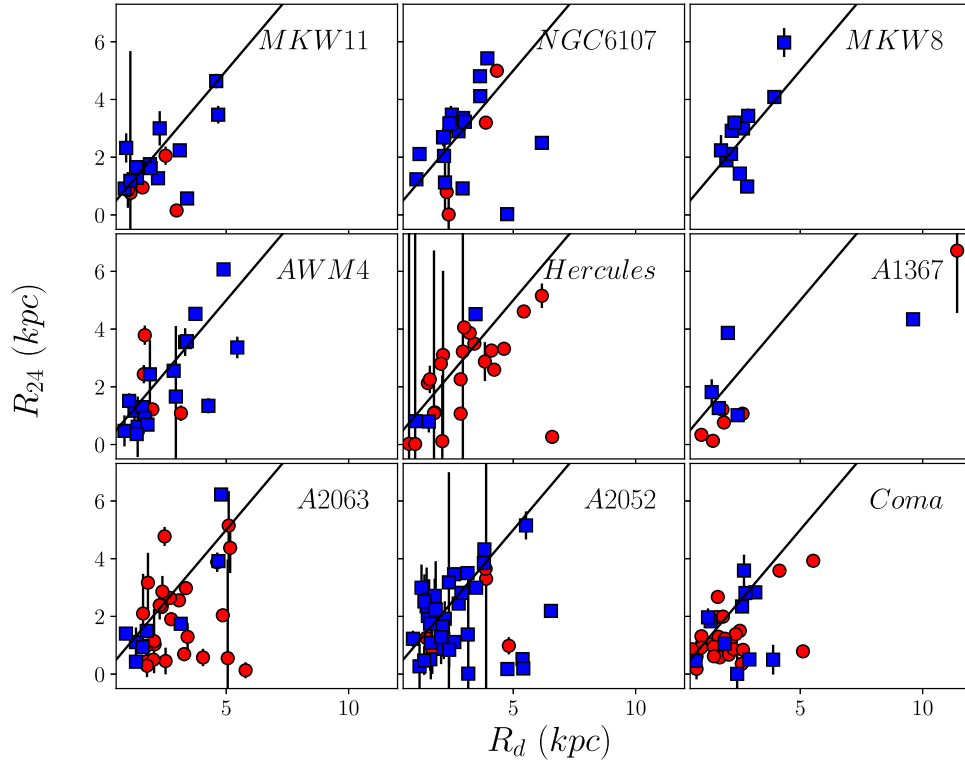
Figure 10. R_{24} versus R_d for all *Local Cluster Survey* clusters. The clusters are ordered left-to-right and top-to-bottom in terms of increasing X-ray luminosity. The solid black line shows a one-to-one correlation. The red circles and blue squares show the core and external galaxies, respectively. For all clusters, the R_{24} is systematically smaller than R_d.
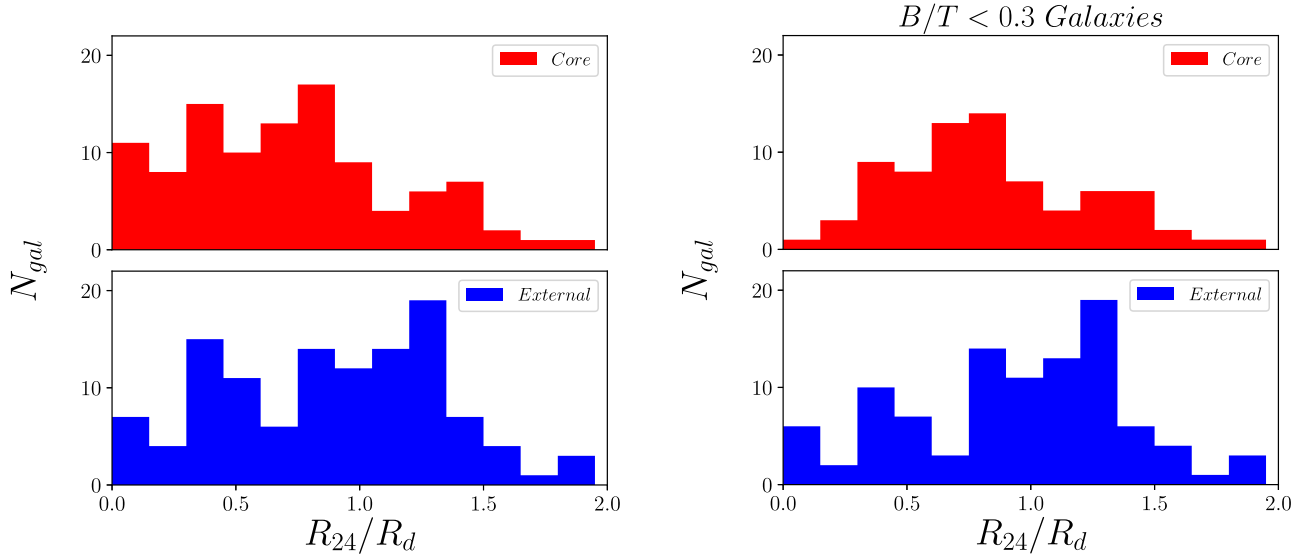
Figure 11. (Left) Distribution of R_{24}/R_d for external (bottom; blue histogram) and core (top; red histogram) galaxies. The distribution of R_{24}/R_d for core galaxies is offset to smaller values compared to the distribution for the external galaxies. (Right) Same as left panel but for $B/T < 0.3$ galaxies only to help control for dependence of R_{24}/R_d on B/T. Again, the core galaxies are offset to smaller values of R_{24}/R_d.

morphology (Dale et al. 2001; Koopmann et al. 2006; Fossati et al. 2013). Some of these discrepancies might be due to differences between samples. For example, the Dale et al. (2001) sample is dominated by late-type spirals, and the galaxies were selected to have strong emission-line features; both of these selection effects could hinder their ability to detect a trend with morphology. Koopmann et al. (2006) do not use the central region of each galaxy when fitting the Hα radial

profiles, due to possible bulge contamination and extinction problems. Thus no galaxies with weak or severely truncated star formation have measured scale lengths. Interestingly, Bretherton et al. (2013) find a correlation between the relative size of the star-forming disk and morphology among field galaxies but not among cluster galaxies. However, we find a correlation between R_{24}/R_d and B/T for both core and external galaxies.
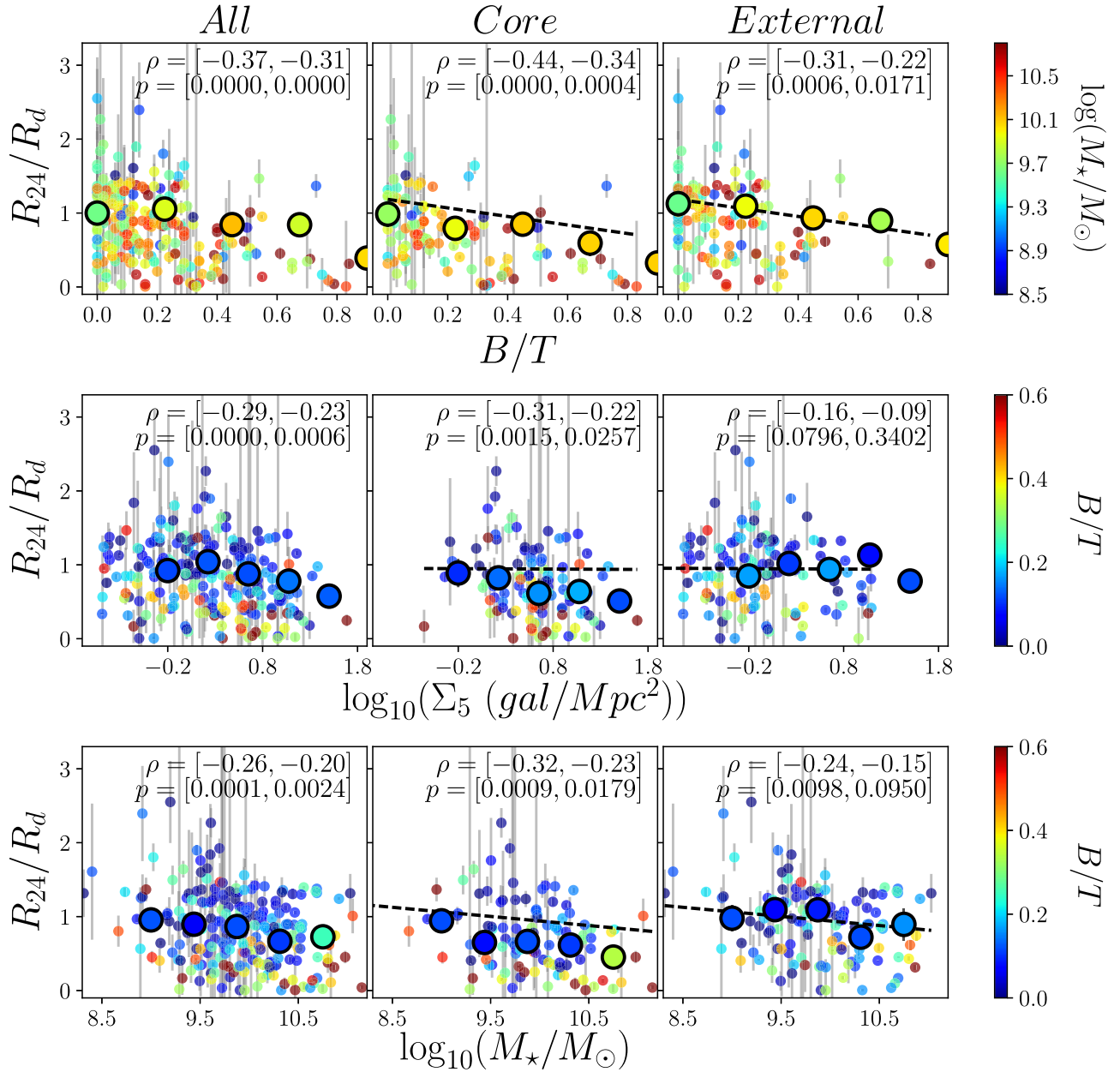
Figure 12. (Top) R_{24}/R_d versus B/T for all (left), core (center), and external galaxies (right). Points are colored according to stellar mass. The 68% confidence interval for the Spearman rank correlation coefficient, ρ, and the corresponding $p-value$ are shown in the upper right. The large points show the median in five equally spaced bins. The black dashed line in the center and right columns is a simple linear fit to the external sample. We show it with the core panel to aid in comparing the samples. (Middle) R_{24}/R_d versus Σ_5. Points are colored according to B/T. R_{24}/R_d and Σ_5 are strongly correlated for the full sample. (Bottom) R_{24}/R_d versus $\log_{10}(M_*/M_\odot)$. The external sample shows a significant anti-correlation between R_{24}/R_d and stellar mass, whereas the core galaxies show a flatter relation.

In the middle panel of Figure 12, we show R_{24}/R_d versus local galaxy density. R_{24}/R_d and Σ_5 are strongly correlated as indicated by a Spearman rank test. A similar effect can be seen in Figure 4; galaxies with smaller R_{24}/R_d ratios are more likely to be found at low projected radii where the projected density of galaxies is high.

Comparison of the core and external panels shows that the core galaxies have lower values of R_{24}/R_d. To further emphasize the offset and to control for the correlation between morphology and environment, we again show the distribution of relative sizes for both core and external galaxies but for $B/T < 0.3$ galaxies only in the right panel of Figure 11.

The core galaxies have R_{24}/R_d ratios that are clearly offset to smaller values.

In the bottom row of Figure 12, we show R_{24}/R_d versus stellar mass, where stellar mass is calculated as described in Moustakas et al. (2013) and assumes a Chabrier IMF (Chabrier 2003). The left column shows the entire GALFIT sample, and the middle and right columns show the core and external samples separately. Using the full sample, we test for a correlation between stellar mass and R_{24}/R_d using a Spearman rank test. The results indicate that R_{24}/R_d and stellar mass are inversely correlated, although the correlation is not particularly strong.
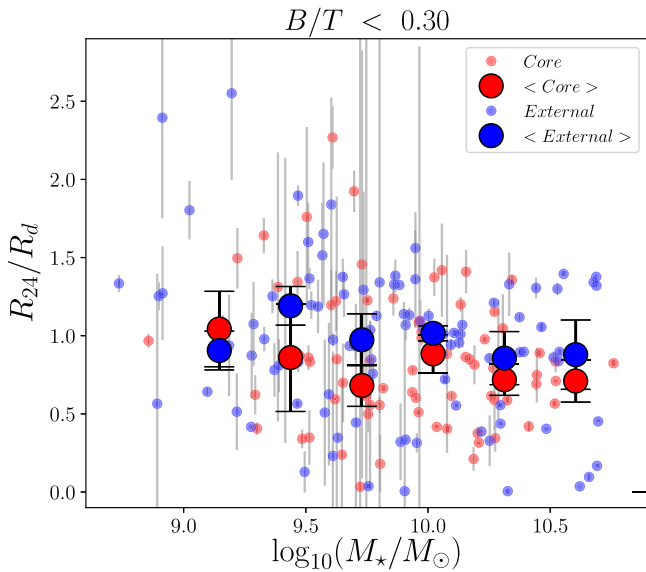
Figure 13. R_{24}/R_d versus stellar mass for core (red) and external (blue) galaxies. We include $B/T < 0.3$ galaxies only to help limit any systematics with B/T. The small points show R_{24}/R_d for individual galaxies, and the large circles show the median in equally spaced bins. The error on the binned points is the 68% confidence interval, which we calculate using bootstrap resampling of the galaxies in each bin. While R_{24}/R_D is systematically lower for the core galaxies, the difference between core and external size ratios does not appear to depend on stellar mass.

We investigate the dependence of R_{24}/R_d on stellar mass further in Figure 13. To control for morphology, we include only the $B/T < 0.3$ galaxies. We show the core galaxies in red and the external galaxies in blue. The large red and blue circles show the median R_{24}/R_d for the core and external samples, respectively, in equally spaced bins. The errorbars show the 68% confidence interval on the median, which we calculate using bootstrap resampling of the galaxies in each bin. While R_{24}/R_d is systematically lower for the core galaxies, the difference between the core and external size ratios does not appear to depend on stellar mass.

We also look at R_{24}/R_d versus several combinations of stellar mass density—namely, stellar mass surface density (Zhang et al. 2013) and M_*/R_e (e.g., Omand et al. 2014). We detect no correlation between R_{24}/R_d and M_*/R_e^2, and a moderate correlation between R_{24}/R_d and M_*/R_e. However, we are testing for a correlation between two correlated variables because both R_{24}/R_d and M_*/R_e have a measure of r-band size in the denominator, and the significance of any detected correlation is thus difficult to interpret.

7.3. Partial Correlation Analysis

The previous section provides convincing evidence that R_{24}/R_d depends on B/T, environment, and stellar mass. However, B/T, environment, and stellar mass are correlated with each other. We attempt to separate the influence of these variables using partial correlation analysis. The partial correlation statistic, which we compute using the ppcor.pcor package in R, indicates the degree to which Y is correlated with X, after removing any correlation between Y and other variables W and Z. The partial correlation coefficient, ρ, can range between -1 and 1 for strongly anti-correlated and correlated variables, respectively. We again account for the error in R_{24}/R_d by creating 1000 realizations of our data, and the mean

and 68% confidence interval for the correlation coefficient and the corresponding statistic are shown in Table 4. The statistic indicates the significance of the corresponding correlation (e.g., 3σ). We highlight the significant correlations in bold.

The results indicate that R_{24}/R_d is correlated with Σ_5 even after controlling for variations in R_{24}/R_d with B/T and stellar mass. Similarly, R_{24}/R_d is correlated with B/T even after controlling for any variations of R_{24}/R_d with Σ_5 and M_*. However, both the Spearman rank and partial correlation tests indicate that R_{24}/R_d is more strongly correlated with B/T than with Σ_5. Interestingly, the partial correlation analysis indicates that R_{24}/R_d is not correlated with stellar mass after variations with B/T and Σ_5 are removed.

7.4. Impact of Coma

Coma is the richest, most X-ray luminous cluster in our sample, and in this section we briefly discuss how the properties of Coma galaxies affect our results. First, we recompute the partial correlation coefficients of R_{24}/R_d, M_*, B/T, and Σ_5 after removing Coma galaxies from our sample. We find that the correlation between R_{24}/R_d and B/T is still significant at the 4.0σ confidence level; B/T remains the most strongly correlated variable with R_{24}/R_d. We detect a less significant (2.4σ) correlation between R_{24}/R_d and Σ_5. R_{24}/R_d and M_* remain uncorrelated when Coma is removed. The results of the partial correlation analysis are summarized in the last two columns of Table 4.

Second, we also compare with distribution of R_{24}/R_d for $B/T < 0.3$ core and external galaxies. The mean (median) R_{24}/R_d for the core and external galaxies is 0.74 ± 0.05 and $0.93 (0.95) \pm 0.05$, respectively, and a KS test indicates that the core and external distributions differ at the 3σ level. Thus, even though the correlation between R_{24}/R_d and Σ_5 weakens when Coma is removed, we still find that the core galaxies have significantly smaller R_{24}/R_d ratios than the external galaxies.

7.5. R_{24}/R_d versus Large-scale Environment

The density of the intra-cluster medium is a key factor in determining the effectiveness with which gas is removed from infalling galaxies by ram-pressure stripping (e.g., Gunn & Gott 1972). We do not have a measure of $\rho_{\rm ICM}$, so we use X-ray luminosity as a proxy. We show R_{24}/R_d for $B/T < 0.3$ cluster galaxies versus the X-ray luminosity of each cluster in Figure 14. Again, we limit the range of B/T in this comparison to help control for the correlation between B/T and environment. We use a box and whisker plot to show the range of values for each cluster. The box extends from the lower to upper quartiles, while the whiskers (errorbars) show the range in each bin. The horizontal line shows the average R_{24}/R_d for the external sample, and the dashed lines show the error in the mean. The MIPS scans for A1367, Hercules, and Coma do not extend to R_{200}. We do not attempt to correct for this, however, because if we try to match the areal coverage of these clusters by selecting a smaller radial cut, we run out of galaxies in other clusters. We repeat the same analysis using X-ray temperature in place of X-ray luminosity, and we find similar results.

Due to the relatively small numbers of galaxies in each cluster, we next look for trends with the large-scale environment by binning the clusters according to X-ray luminosity or velocity dispersion. We combine the galaxy groups ($\sigma < 700\,{\rm km\,s^{-1}}$: MKW11, MKW8, AWM4, and NGC6107) and clusters

Table 3
Definition of Radial Size Symbols

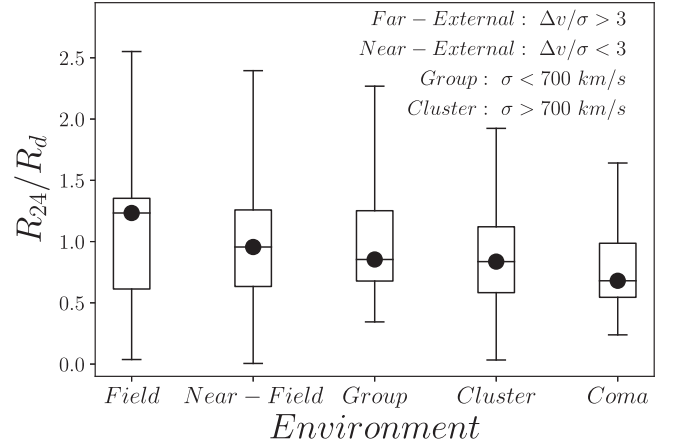| Symbol	Definition
R_{24}	24 μm half-light radius from GALFIT single-component *Sérsic* model
R_e	*r*-band half-light radius from GIM2D single-component *Sérsic* model (Simard et al. 2011)
R_d	*r*-band half-light radius of disk component based on two-component GIM2D model with $n = 4$ bulge + exponential disk (Simard et al. 2011)

Table 4
Summary of Partial Correlation Analysis

	With Coma ($N = 224$)				Without Coma ($N = 192$)			
	ρ	Conf. Interval	Significance	Conf. Interval	ρ	Conf. Interval	Significance	Conf. Interval
$R_{24}/R_d - M_*$	−0.16	[−0.19, −0.12]	2.4	[2.9, 1.9]	−0.13	[−0.17, −0.09]	1.9	[2.4, 1.3]
$R_{24}/R_d - B/T$	**−0.29**	[−0.32, −0.26]	**4.5**	[5.1, 3.9]	**−0.28**	[−0.32, −0.24]	**4.0**	[4.6, 3.3]
$R_{24}/R_d - \Sigma_5$	**−0.24**	[−0.28, −0.21]	**3.7**	[4.3, 3.2]	−0.17	[−0.21, −0.13]	2.4	[2.9, 1.8]
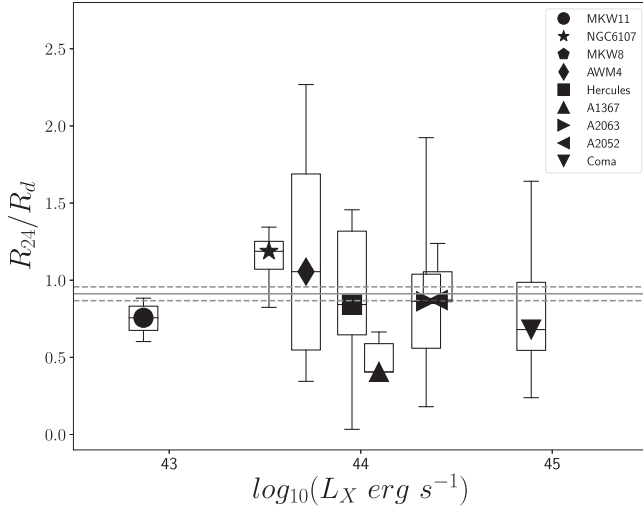
Figure 14. R_{24}/R_d of $B/T < 0.3$ galaxies versus the X-ray luminosity of cluster. The individual points show the median value, the box marks the range between the upper and lower quartiles, and the whiskers show the full range of values for each group/cluster. The horizontal line shows the average R_{24}/R_d for the field galaxies, and the dashed lines show the error in the mean.

Figure 15. Median R_{24}/R_d of $B/T < 0.3$ galaxies versus large-scale environment. The boxes show first and third quartiles, and the whiskers or errorbars show the range of the data in each bin. Here we split the external sample into near-external ($\Delta v/\sigma < 3$) and the far-external ($\Delta v/\sigma > 3$). We divide the clusters by velocity dispersion, defining groups as $\sigma < 700$ km s^{-1}. We leave Coma in a class by itself.

($\sigma > 700$ km s^{-1}: Hercules, Abell 1367, Abell 2052, and Abell 2063), and leave Coma in a class by itself. For this comparison only, we separate the external sample into near-external and far-external galaxies, where the near-external galaxies have $\Delta v/\sigma < 3$. These galaxies likely live in the large-scale structure surrounding the clusters and may already be affected by environmental process. The far-external galaxies have $\Delta v/\sigma > 3$ and are more likely to be isolated from the cluster environment. We show the median R_{24}/R_d for $B/T < 0.3$ galaxies versus global environment in Figure 15. Again, we use a box and whisker plot to show the inner quartiles and range of the data. The median R_{24}/R_d decreases as the environmental density increases from the field through to Coma. In addition, the galaxy groups and lower-mass clusters have median R_{24}/R_d that falls between the near-field and Coma, but the differences are not statistically significant. While our results suggest that cluster mass is important, a larger sample of groups and clusters is needed to explore variations between R_{24}/R_d and cluster/group

mass. Not many studies have measured R_{24}/R_d as a function of cluster mass or X-ray luminosity. Dale et al. (2001) make a preliminary attempt to measure the effect of cluster X-ray luminosity on stripping, and they find no systematic trend.

7.6. R_{24}/R_d versus H I Content

All of the clusters in our sample lie within the ALFALFA survey (Giovanelli et al. 2005). ALFALFA maps H I to a resolution of 3′.5 and with a pointing accuracy better than 30″ for sources with S/N > 6.5, and a total of 43 galaxies in the GALFIT sample have H I detections. We calculate H I mass for these galaxies according to the following relation:

$$M_{H\,I} = 2.36 \times 10^5 \, D^2 \int F dV \; M_\odot, \qquad (1)$$

where D is the distance in Mpc and $\int F dV$ is the total H I line flux in Jy km s^{-1} (e.g., Wild 1952; Roberts 1962). In the left panel of Figure 16, we show R_{24}/R_d versus H I mass fraction $M_{H\,I}/M_*$. The squares and circles show external and core
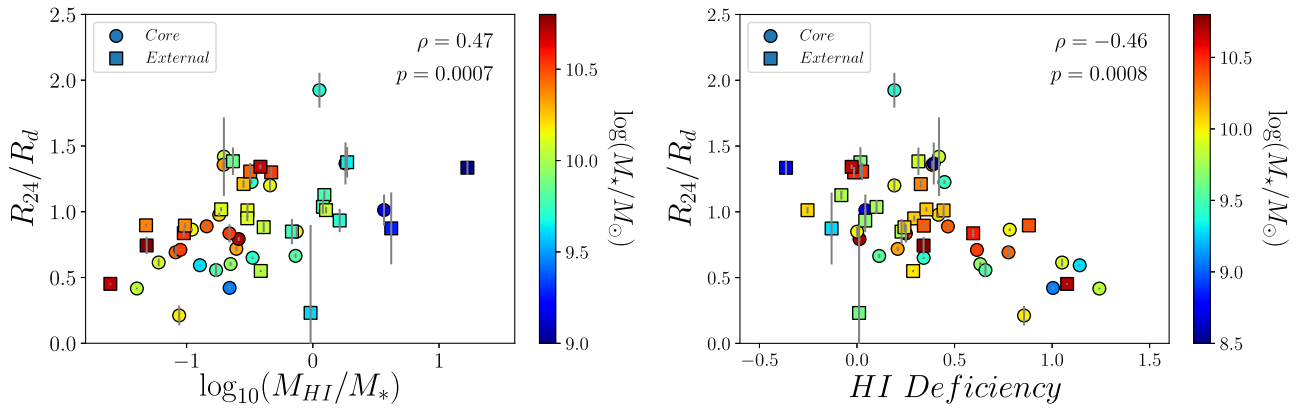
Figure 16. (Left) R_{24}/R_d versus H I mass fraction. The data show a significant ($>3\sigma$) correlation between R_{24}/R_d and H I mass fraction. (Right) R_{24}/R_d versus H I deficiency. The data show a significant ($>3\sigma$) anti-correlation between R_{24}/R_d and H I deficiency in the sense that galaxies with smaller R_{24}/R_d also have less H I gas than isolated galaxies.

galaxies, respectivly, and the color indicates stellar mass. A Spearman rank test indicates that the two quantities are strongly correlated; galaxies with smaller values of R_{24}/R_d have a smaller H I mass fraction.

Another common way to describe the gas content of spiral galaxies is with H I deficiency (Haynes & Giovanelli 1984; Toribio et al. 2011). This compares the H I content of a galaxy to the H I content of isolated field galaxies of comparable size, and positive values of deficiency indicate that a galaxy has *less* H I gas than a field galaxy of comparable size (Haynes & Giovanelli 1984; Toribio et al. 2011). We calculate H I deficiency according to the relationship presented in Toribio et al. (2011), using the isophotal *r*-band diameter from SDSS to measure size. In Figure 16 we show R_{24}/R_d versus H I deficiency. The data show a significant (3.5σ) anti-correlation in the sense that galaxies with smaller R_{24}/R_d also have less H I gas than isolated galaxies of comparable size. We are not able to confirm that the converse (i.e., that H I deficient galaxies will have small R_{24}/R_d ratios) is true; H I deficient galaxies with widespread but low levels of star formation would likely fall below our surface-brightness cut. Figure 16 also shows that core galaxies tend to have lower H I mass fractions and higher H I deficiencies than external galaxies.

Our findings are consistent with previous studies. The $H\alpha$ 3 survey of nearby galaxies (Fossati et al. 2013; Gavazzi et al. 2013) and Koopmann and Kenney (2004b) for Virgo galaxies find that the relative size of the $H\alpha$ disk is inversely correlated with H I deficiency. In addition, infrared and CO observations of Virgo galaxies show that H I deficient spirals have smaller dust and molecular gas disks (Cortese et al. 2010; Boselli et al. 2011).

7.7. R_{24}/R_d versus Color

If Figure 17 we show NUV $- r$ versus R_{24}/R_d, and the points are color-coded by B/T. The core and external galaxies are shown in the middle and right panels, respectively. The horizontal solid line in each panel marks NUV $- r = 4$, a rough dividing line between blue and red galaxies (e.g., Salim et al. 2007), and the dashed horizontal lines mark the region of the green valley (e.g., Wyder et al. 2007). As before, to account for the variation in error among the individual 24 μm best-fit models, we create 1000 Monte-Carlo realizations of the data
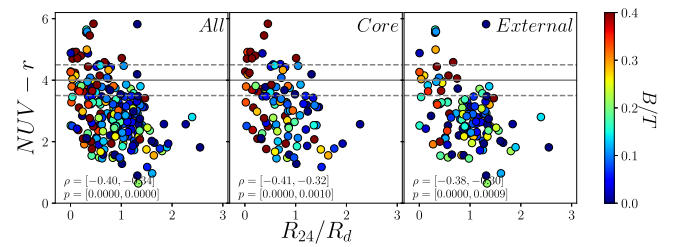
Figure 17. NUV $- r$ versus R_{24}/R_d color for all (left panel), core (middle panel), and external (right panel) galaxies. The points are colored by B/T. The horizontal solid line in each panel marks NUV $- r = 4$, a rough dividing line between blue and red galaxies (e.g., Salim et al. 2007), and the dashed horizontal lines mark the region of the green valley (e.g., Wyder et al. 2007). Galaxies with redder NUV $- r$ colors have smaller values of R_{24}/R_d.

and calculate the Spearman rank correlation coefficient for each realization, assuming that the GALFIT errors for R_{24} are normally distributed. The numbers in Figure 17 show the 68% confidence interval for the correlation coefficient (ρ) and the probability of no correlation (p). R_{24}/R_d is strongly inversely correlated with NUV $- r$ color ($>5\sigma$ for the combined core +external sample); galaxies that have red NUV $- r$ colors and thus low NUV specific star formation rates have more centrally concentrated star formation.

8. Discussion

Our goal is to investigate the spatial distribution of star formation in galaxies that have been accreted into a cluster but are still forming stars. In Figures 11–15, we show that star-forming galaxies in dense environments have more centrally concentrated star formation. Models of environmentally driven depletion predict that gas is preferentially removed from the outskirts of galaxies (e.g., Gunn & Gott 1972; Kawata & Mulchaey 2008; Bekki 2014), and our observations of smaller star-forming disks in denser environments support this. In addition, we find that galaxies with smaller star-forming disks are more H I deficient (Figure 16) and have redder colors (Figure 17), suggesting that smaller star-forming disks are indicative of the transition phase between blue, gas-rich and red, depleted galaxies.

Centrally concentrated star formation should lead to an increase in B/T, as suggested by Bösch et al. (2013). We can estimate the further evolution of the bulge-to-total ratio for the green valley galaxies if we assume a typical gas mass fraction of 10% (from Figure 16 for galaxies with $R_{24}/R_d \approx 0.5$). If we assume a current $B/T = 0.2$ and $M/L = 1$, the B/T would increase to 0.3 after all the gas is consumed. This is not a huge effect. However, atomic gas is easier to strip than molecular gas (e.g., Boselli et al. 2014), and so our estimate is likely a lower limit on the final bulge-to-total ratio. We could better predict the growth of the central bulge if we obtain molecular gas masses for the *Local Cluster Survey* galaxies.

8.1. Outside-in Quenching Timescale

The timescale over which R_{24}/R_d decreases in an important parameter that can help identify the physical mechanism that is causing outside-in quenching. We construct a simple model to constrain this timescale using the observed distribution of R_{24}/R_d for the core and external samples and simulations of cluster infall. Our model assumes that the size of the star-forming disk decreases linearly with time once a galaxy is accreted into a cluster. The distribution of R_{24}/R_d for the core galaxies results from the modification of the external R_{24}/R_d distribution as follows:

$$\left(\frac{R_{24}}{R_d}\right)_{\text{core}} = \left(\frac{R_{24}}{Rd}\right)_{\text{external}} \times \frac{dr}{dt} \times t_{\text{infall}}, \quad (2)$$

where t_{infall} is the time since accretion into the cluster, and dr/dt is the rate at which the size of the star-forming disk is decreasing in the cluster environment. We assume dr/dt is the same for all galaxies and that the distribution of R_{24}/R_d in the external sample is comparable to that of the core galaxies at the time of infall. (While field galaxies at the time of infall likely had higher star formation rates due to the correlation of galaxy star formation rates with redshift [e.g., Madau & Dickinson 2014, and references therein], there is no compelling evidence to suggest that R_{24}/R_d is larger for intermediate redshift galaxies [e.g., Nelson et al. 2016].) For each galaxy in the external sample, we assign an infall time as αt_{max}, where α is a random number between zero and 1. In effect, this assumes that the accretion rate is uniform over the time t_{max}, which is a reasonable approximation to theoretical mass accretion histories for $t_{\text{max}} < 5$ Gyr (e.g., Neistein & Dekel 2008). To be conservative, we let t_{max}, the time period over which the star-forming core galaxies have been accreted, range from 1 to 4 Gyr. We note that both the phase space distribution of the core galaxies (e.g., Oman et al. 2013) and simulations of the mass accretion history of clusters (e.g., McGee et al. 2009) suggest that $t_{\text{max}} \simeq 3$–4 Gyr for the star-forming core galaxies.

To quantify the timescale, we step dr/dt from −2 to zero and calculate the expected distribution of R_{24}/R_d for the core sample according to Equation (2). We compare the resulting distribution of sizes to that of the observed core sample, and compute the probability that the two are drawn from the same population using a Kolmogorov–Smirnov test. For a given value of dr/dt, we repeat the comparison 1000 times, generating a new set of infall times for each trial. We show the distribution of resulting K-S test p-values versus dr/dt in Figure 18, and p-values near 1 indicate that the simulated distribution of R_{24}/R_d is similar to the observed distribution.
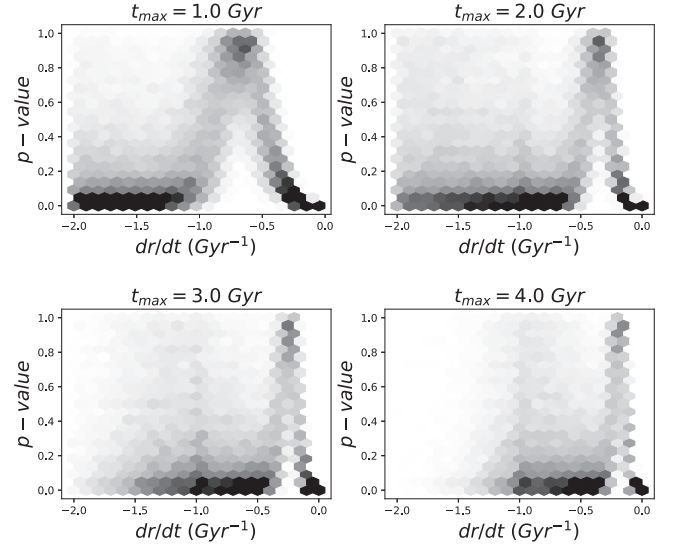
Figure 18. We create a simple model where R_{24}/R_d of the external sample decreases uniformly at a rate of dr/dt once a galaxy is accreted into a cluster. We vary dr/dt from −2 to 0 Gyr⁻¹, and transform the R_{24}/R_d of the external sample by randomly assigning infall times to each galaxy (1000 realizations per dr/dt value). We compare the simulated distribution of R_{24}/R_d with the observed distribution of the core sample using a K-S test. We show the distribution of K-S test probability values versus dr/dt. The four panels show the results as we allow the accretion timescale for the core sample to increase from 1 to 4 Gyr. For all accretion times, $|dr/dt| < 1$, implying a long (>1 Gyr) timescale for removing the star-forming disk.

For $t_{\text{max}} = 1$ Gyr, dr/dt peaks near -0.6 Gyr⁻¹, and the star-forming disk would be removed in ~ 1.7 Gyr. For $t_{\text{max}} = 4$ Gyr, dr/dt peaks near -0.2 Gyr⁻¹, and the star-forming disks would be completely removed in 5 Gyr. Thus, while a precise estimate of the disk-shrinking time requires a careful comparison with simulations of cluster growth, our simplified model suggests that for a reasonable estimate of infall times, the disk-shrinking timescale is greater than 1 Gyr and likely greater than 2 Gyr.

This timescale has significant implications for the delay +rapid quenching model of Wetzel et al. (2012, 2013). First, our estimated timescale is significantly longer than expected for the fast-quenching phase of Wetzel et al. (2013). Second, we show that galaxies undergo a significant transformation during the delay phase, in contrast with the delay+rapid model as originally proposed, in which the galaxies remain unchanged in the period before the rapid quenching event.

8.2. The Effect of B/T on Quenching

At this point, we do not have a satisfactory explanation for why B/T is inversely correlated with R_{24}/R_d. One mechanism that could explain the link between morphology and star formation properties of spirals is morphological quenching: the presence of a bulge stabilizes the gas in a disk, and this prevents gravitational collapse and star formation (e.g., Martig et al. 2009). However, it is not clear that this would lead to more concentrated star formation, and many of our galaxies with high B/T were not detected in H I, which implies that they have lower gas masses rather than a reservoir of gas that never formed stars. Simulations provide conflicting results. Steinhauser et al. (2012) and McCarthy et al. (2008) show that more concentrated galaxies are better able to retain their gas in dense environments, which seems at odds with our results,

while Jáchym et al. (2007) show that galaxies with larger bulge fractions lose more gas.

One plausible explanation of the link between B/T and R_{24}/R_d comes from Solanes et al. (2001). In an extensive study of H I in clusters, they find that early-type spirals are more likely to be H I deficient than Sbc-Sc spirals. The discrepancy persists out to projected radii of ≈ 4 Mpc but not farther, which shows that this is likely the result of an environmental rather than secular process. Solanes et al. (2001) point out that the central H I depressions observed in some early-type spirals could amplify the effect of ram-pressure stripping, as shown by Moore et al. (1999). This could imply that the trend in R_{24}/R_d with morphology arises because high B/T galaxies are more susceptible to ram-pressure stripping. Future simulations may provide insight into how the bulge fraction of a spiral affects its ability to retain gas in dense environments.

9. Summary

We present 24 μm size measurements for 224 galaxies in nine nearby galaxy groups and clusters. We normalize the 24 μm effective radius by the disk scale length (Simard et al. 2011) and look for variations in this ratio as a function of morphology, environment, and stellar mass. Our primary results are that (1) R_{24}/R_d is strongly correlated with morphology for star-forming galaxies in the sense that galaxies with higher bulge-to-total ratios or larger *Sérsic* indices have more centrally concentrated star formation, and (2) star-forming galaxies in more dense environments have more centrally concentrated star formation than galaxies in less dense environments with similar mass and B/T. Furthermore, we find that galaxies with smaller star-forming disks tend to have lower H I mass fractions and redder $NUV - r$ colors, suggesting that at least some galaxies experience a decline in R_{24}/R_d as they transition from blue to red.

We do not detect any trend in the median R_{24}/R_d ratio of cluster galaxies versus X-ray luminosity of the host galaxy cluster. However, when we bin our sample by environment and control for the morphology–density relation by using only $B/T < 0.3$ galaxies, we do see a trend with large-scale environment that suggests that R_{24}/R_d is highest in the field, lower in our low-mass clusters and groups, and lower still in the extreme environment within the Coma cluster.

We build a toy model to constrain the timescale over which the star-forming disks shrink in the cluster environment. When allowing the galaxies to enter the cluster with a realistic range of infall histories, we find that the star-forming disks in our sample will shrink on a timescale longer than 1 Gyr and likely longer than 2 Gyr.

Our results provide a new piece of information on what is happening to galaxies after they have been accreted by a cluster but while they are still able to form stars. In the context of recent hybrid models of environmental quenching (e.g., Wetzel et al. 2012; Balogh et al. 2016), our core galaxies are considered to be in the delay phase, the period between being accreted into the cluster and complete quenching of star formation. We present clear evidence that the spatial distribution of star formation becomes more concentrated during this delay phase. Our results suggest that the quenching timescale is long (>2 Gyr), which is consistent with mechanisms such as the removal of halo gas through starvation (e.g., Larson et al. 1980) and the slow removal of cold disk gas through extended ram-pressure stripping.

Appendix
GALFIT Simulations

The MIPS data have lower resolution and lower signal-to-noise ratios than the optical imaging that GALFIT is typically used with; at the median redshift of our cluster sample, 1 pixel on the MIPS camera corresponds to 1.48 kpc. To test the reliability of the GALFIT models, we create 200 model galaxies on each MIPS scan and run them through our analysis. The model galaxies consist of single-component *Sérsic* models with randomly selected parameters, and the range of parameters are as follows. The effective radius is varied uniformly from $1.''23$ to $20''$, the *Sérsic* index is varied uniformly from 0.5 to 4, and the magnitude is varied uniformly from 11.5 to 16. The model galaxy is created by first selecting a region on the MIPS scan that does not have a nearby object within 15 pixels. We create a cutout of this region, generate a model galaxy using GALFIT, and then add the model and noise to the MIPS cutout. The PRF may vary across the final MIPS scan; to incorporate this effect in our simulations, we vary the PRF used to create the model galaxy by randomly selecting from one of the five brightest point sources on each image. We then run GALFIT on the simulated galaxy to compare the recovered versus input parameters. GALFIT requires an initial estimate of the model parameters; we use the model parameters with 20% uncertainty added to the input parameters, except that we keep the axis ratio and position angle fixed to reproduce our fitting procedure. When detecting the galaxy, we use the PRF that we use when modeling the real galaxies (except for Hercules; see below).

We show the results of the simulations in Figure 19, where we plot the ratio of the recovered to input effective radius versus measured surface brightness. We calculate the observed surface brightness, μ, as

$$\mu = m + 2.5 \log_{10}(\pi R_{e(\text{obs})}^2 \, B/A), \qquad (3)$$

where m, $R_{e(\text{obs})}$, and B/A are the magnitude, effective radius, and axis ratio of the best-fit *Sérsic* model. (Area of ellipse is $A = \pi ab$.) In each panel, the scatter in the recovered size increases significantly beyond a surface brightness of ~ 20 mag/arcsec^2. We give the average and standard deviation
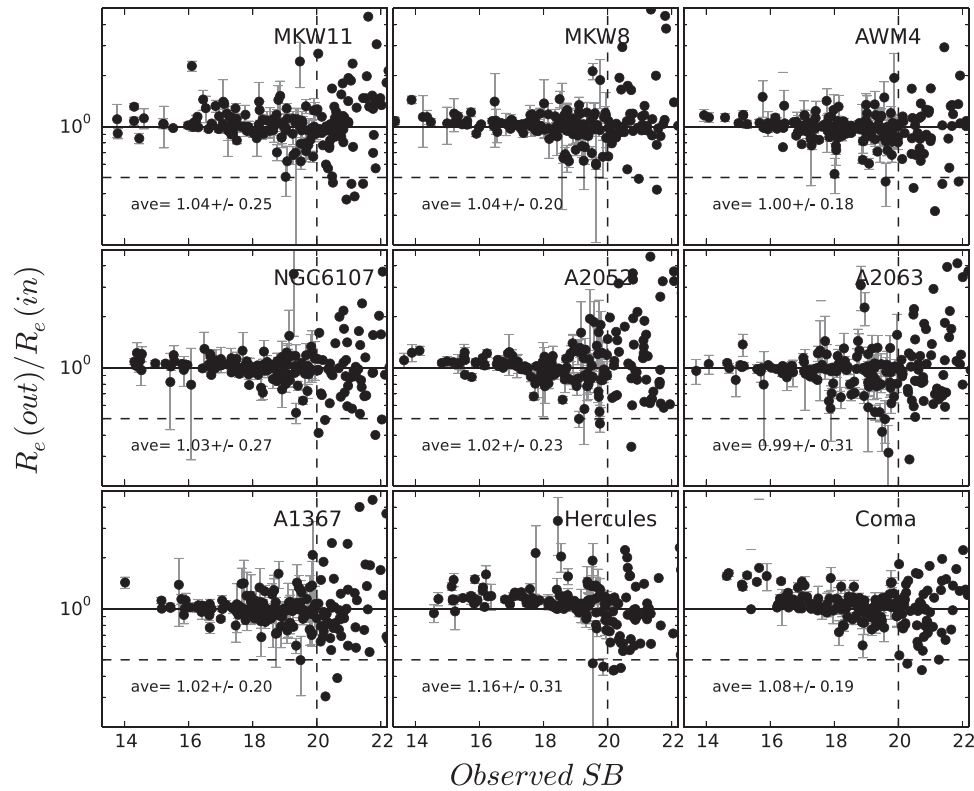
Figure 19. Ratio of recovered to input R_e of simulated galaxies versus observed surface brightness. The solid horizontal light shows a ratio of one. The dashed vertical line shows the surface brightness limit applied to each cluster mosaic image, beyond which the fits become unacceptably inaccurate. The average and standard deviation are shown in each panel for all galaxies to the left of the dashed vertical line.

of the recovered to input R_e for images with $\mu > 20$. These are consistent with a ratio of one, indicating that GALFIT is able to recover the size of the simulated galaxies with $\mu > 20$.

In Figure 20 we show the ratio of the recovered to input effective radius versus the effective radius of the input model, just for the models that meet the surface brightness cuts illustrated in Figure 19. The vertical dashed line corresponds to the $2\overset{''}{.}45$-pixel scale of the MIPS scans. Our convolved models are able to recover the input R_e to this limit, although the recovered values for Hercules are systematically and significantly larger than the input values. When we tried to create a PRF from a source on the Hercules scan, the recovered radii were 20%–30% larger than the input values. When we use the PRF from *Spitzer Science Center*, the recovered radii are still systematically high, but only by 16%, as shown in Figure 19. The remaining offset is likely due to a mismatch in PRF, but we are not able to further correct for this. The simulations indicate that we will be biased toward measuring larger 24 μm R_e in Hercules.

The simulation results lead us to apply a surface brightness cut to our sample. In addition to the selection criteria listed in Section 4, we keep only those galaxies whose measured surface brightness is above $\mu < 20$ mag/sq arcsec. In physical units, this surface brightness cut corresponds to $\approx$0.012 $M_\odot$ yr^{-1} kpc^{-2} or 7×10^7 erg s^{-1} kpc^{-2}.
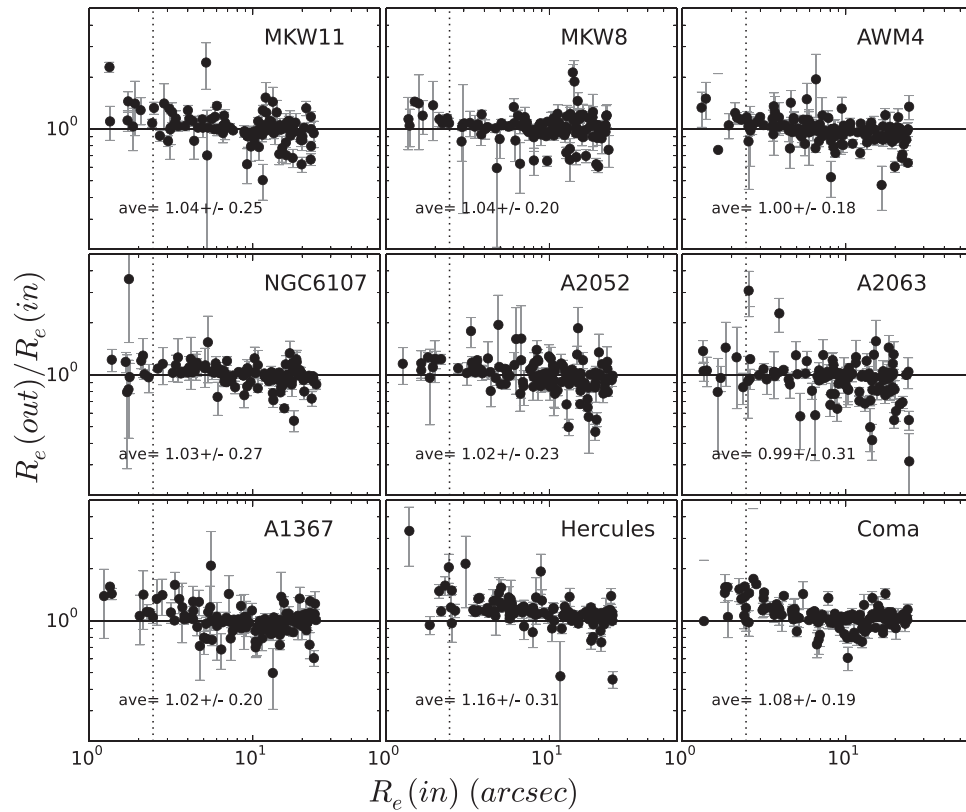
Figure 20. Recovered versus input galaxy R_e for simulated galaxies. Only galaxies with measured surface brightness $\mu > 20$ are shown. The average ratio of recovered to input radius is shown, and the error is the standard deviation. For all clusters, with the exception of Hercules and Coma, the recovered sizes are consistent with the input sizes. Hercules, and Coma to a lesser extent, have recovered sizes that are systematically larger than the input size.

ORCID iDs

Rose A. Finn ⓘ https://orcid.org/0000-0001-8518-4862
Vandana Desai ⓘ https://orcid.org/0000-0002-1340-0543
Gregory Rudnick ⓘ https://orcid.org/0000-0001-5851-1856
Martha P. Haynes ⓘ https://orcid.org/0000-0001-5334-5166
Bianca Poggianti ⓘ https://orcid.org/0000-0001-8751-8360
Dennis Zaritsky ⓘ https://orcid.org/0000-0002-5177-727X

References

Bahé, Y. M., McCarthy, I. G., Balogh, M. L., & Font, A. S. 2013, MNRAS, 430, 3017
Baldry, I. K., Balogh, M. L., Bower, R. G., et al. 2006, MNRAS, 373, 469
Balogh, M., Eke, V., Miller, C., et al. 2004, MNRAS, 348, 1355
Balogh, M. L., McGee, S. L., Mok, A., et al. 2016, MNRAS, 456, 4364
Balogh, M. L., Morris, S. L., Yee, H. K. C., Carlberg, R. G., & Ellingson, E. 1997, ApJL, 488, L75
Balogh, M. L., Morris, S. L., Yee, H. K. C., Carlberg, R. G., & Ellingson, E. 1999, ApJ, 527, 54
Balogh, M. L., Navarro, J. F., & Morris, S. L. 2000, ApJ, 540, 113
Bamford, S. P., Milvang-Jensen, B., & Aragón-Salamanca, A. 2007, MNRAS, 378, L6
Beers, T. C., Flynn, K., & Gebhardt, K. 1990, AJ, 100, 32
Bekki, K. 2014, MNRAS, 438, 444
Bendo, G. J., Calzetti, D., Engelbracht, C. W., et al. 2007, MNRAS, 380, 1313
Bertin, E., & Arnouts, S. 1996, A&AS, 117, 393
Blanton, M. R., Kazin, E., Muna, D., Weaver, B. A., & Price-Whelan, A. 2011, AJ, 142, 31
Bösch, B., Böhm, A., Wolf, C., et al. 2013, A&A, 549, A142
Boselli, A., Boissier, S., Heinis, S., et al. 2011, A&A, 528, A107
Boselli, A., Cortese, L., Boquien, M., et al. 2014, A&A, 564, A67
Bretherton, C. F., Moss, C., & James, P. A. 2013, A&A, 553, A67
Calzetti, D., Kennicutt, R. C., Engelbracht, C. W., et al. 2007, ApJ, 666, 870

Chabrier, G. 2003, PASP, 115, 763
Chary, R., & Elbaz, D. 2001, ApJ, 556, 562
Cortese, L., Davies, J. I., Pohlen, M., et al. 2010, A&A, 518, L49
Dale, D. A., Giovanelli, R., Haynes, M. P., Hardy, E., & Campusano, L. E. 2001, AJ, 121, 1886
De Lucia, G., Weinmann, S., Poggianti, B. M., Aragón-Salamanca, A., & Zaritsky, D. 2012, MNRAS, 423, 1277
Dressler, A., & Gunn, J. E. 1983, ApJ, 270, 7
Ellingson, E., Lin, H., Yee, H. K. C., & Carlberg, R. G. 2001, ApJ, 547, 609
Finn, R. A., Balogh, M. L., Zaritsky, D., Miller, C. J., & Nichol, R. C. 2008, ApJ, 679, 279
Finn, R. A., Desai, V., Rudnick, G., et al. 2010, ApJ, 720, 87
Finn, R. A., Zaritsky, D., McCarthy, D. W., Jr., et al. 2005, ApJ, 630, 206
Fossati, M., Gavazzi, G., Savorgnan, G., et al. 2013, A&A, 553, A91
Fossati, M., Wilman, D. J., Mendel, J. T., et al. 2017, ApJ, 835, 153
Gallazzi, A., Bell, E. F., Wolf, C., et al. 2009, ApJ, 690, 1883
Gavazzi, G., Fumagalli, M., Fossati, M., et al. 2013, A&A, 553, A89
Giovanelli, R., Haynes, M. P., Kent, B. R., et al. 2005, AJ, 130, 2598
Gómez, P. L., Nichol, R. C., Miller, C. J., et al. 2003, ApJ, 584, 210
Gunn, J. E., & Gott, J. R., III 1972, ApJ, 176, 1
Haines, C. P., Pereira, M. J., Smith, G. P., et al. 2013, ApJ, 775, 126
Haines, C. P., Pereira, M. J., Smith, G. P., et al. 2015, ApJ, 806, 101
Haynes, M. P., & Giovanelli, R. 1984, AJ, 89, 758
Hodge, P. W., & Kennicutt, R. C., Jr. 1983, ApJ, 267, 563
Jáchym, P., Palouš, J., Köppen, J., & Combes, F. 2007, A&A, 472, 5
Jaffé, Y. L., Aragón-Salamanca, A., Kuntschner, H., et al. 2011, MNRAS, 417, 1996
Kauffmann, G., Heckman, T. M., Tremonti, C., et al. 2003, MNRAS, 346, 1055
Kawata, D., & Mulchaey, J. S. 2008, ApJL, 672, L103
Kimm, T., Somerville, R. S., Yi, S. K., et al. 2009, MNRAS, 394, 1131
Knobel, C., Lilly, S. J., Woo, J., & Kovač, K. 2015, ApJ, 800, 24
Koopmann, R. A., Haynes, M. P., & Catinella, B. 2006, AJ, 131, 716
Koopmann, R. A., & Kenney, J. D. P. 1998, ApJL, 497, L75
Koopmann, R. A., & Kenney, J. D. P. 2004a, ApJ, 613, 851
Koopmann, R. A., & Kenney, J. D. P. 2004b, ApJ, 613, 866
Larson, R. B., Tinsley, B. M., & Caldwell, C. N. 1980, ApJ, 237, 692

Lewis, I., Balogh, M., De Propris, R., et al. 2002, MNRAS, 334, 673
Lin, L., Jian, H.-Y., Foucaud, S., et al. 2014, ApJ, 782, 33
Madau, P., & Dickinson, M. 2014, ARA&A, 52, 415
Mahdavi, A., & Geller, M. J. 2001, ApJL, 554, L129
Martig, M., Bournaud, F., Teyssier, R., & Dekel, A. 2009, ApJ, 707, 250
McCarthy, I. G., Frenk, C. S., Font, A. S., et al. 2008, MNRAS, 383, 593
McGee, S. L., Balogh, M. L., Bower, R. G., Font, A. S., & McCarthy, I. G. 2009, MNRAS, 400, 937
McGee, S. L., Balogh, M. L., Wilman, D. J., et al. 2011, MNRAS, 413, 996
Mok, A., Balogh, M. L., McGee, S. L., et al. 2013, MNRAS, 431, 1090
Mok, A., Balogh, M. L., McGee, S. L., et al. 2014, MNRAS, 438, 3070
Moore, B., Lake, G., Quinn, T., & Stadel, J. 1999, MNRAS, 304, 465
Moss, C., & Whittle, M. 2000, MNRAS, 317, 667
Moustakas, J., Coil, A. L., Aird, J., et al. 2013, ApJ, 767, 50
Muzzin, A., Marchesini, D., Stefanon, M., et al. 2013, ApJ, 777, 18
Muzzin, A., van der Burg, R. F. J., McGee, S. L., et al. 2014, ApJ, 796, 65
Neistein, E., & Dekel, A. 2008, MNRAS, 383, 615
Nelson, E. J., van Dokkum, P. G., Förster Schreiber, N. M., et al. 2016, ApJ, 828, 27
Oman, K. A., & Hudson, M. J. 2016, MNRAS, 463, 3083
Oman, K. A., Hudson, M. J., & Behroozi, P. S. 2013, MNRAS, 431, 2307
Omand, C. M. B., Balogh, M. L., & Poggianti, B. M. 2014, MNRAS, 440, 843
Peng, C. Y., Ho, L. C., Impey, C. D., & Rix, H.-W. 2002, AJ, 124, 266
Peng, Y.-j., Lilly, S. J., Kovač, K., et al. 2010, ApJ, 721, 193
Poggianti, B. M., Desai, V., Finn, R., et al. 2008, ApJ, 684, 888
Poggianti, B. M., Smail, I., Dressler, A., et al. 1999, ApJ, 518, 576
Postman, M., Franx, M., Cross, N. J. G., et al. 2005, ApJ, 623, 721
Rieke, G. H., Young, E. T., Engelbracht, C. W., et al. 2004, ApJS, 154, 25
Roberts, M. S. 1962, AJ, 67, 437
Rodríguez del Pino, B., Aragón-Salamanca, A., Chies-Santos, A. L., et al. 2017, MNRAS, 467, 4200
Salim, S., Rich, R. M., Charlot, S., et al. 2007, ApJS, 173, 267
Schaefer, A. L., Croom, S. M., Allen, J. T., et al. 2017, MNRAS, 464, 121
Simard, L., Mendel, J. T., Patton, D. R., Ellison, S. L., & McConnachie, A. W. 2011, ApJS, 196, 11
Solanes, J. M., Manrique, A., García-Gómez, C., et al. 2001, ApJ, 548, 97
Steinhauser, D., Haider, M., Kapferer, W., & Schindler, S. 2012, A&A, 544, A54
Stern, D., Assef, R. J., Benford, D. J., et al. 2012, ApJ, 753, 30
Taranu, D. S., Hudson, M. J., Balogh, M. L., et al. 2014, MNRAS, 440, 1934
Toribio, M. C., Solanes, J. M., Giovanelli, R., Haynes, M. P., & Martin, A. M. 2011, ApJ, 732, 93
Tran, K.-V. H., Franx, M., Illingworth, G. D., et al. 2007, ApJ, 661, 750
van der Burg, R. F. J., Muzzin, A., Hoekstra, H., et al. 2013, A&A, 557, A15
Vulcani, B., Poggianti, B. M., Finn, R. A., et al. 2010, ApJL, 710, L1
Wetzel, A. R., Tinker, J. L., & Conroy, C. 2012, MNRAS, 424, 232
Wetzel, A. R., Tinker, J. L., Conroy, C., & van den Bosch, F. C. 2013, MNRAS, 432, 336
Wild, J. P. 1952, ApJ, 115, 206
Wolf, C., Aragón-Salamanca, A., Balogh, M., et al. 2009, MNRAS, 393, 1302
Wyder, T. K., Martin, D. C., Schiminovich, D., et al. 2007, ApJS, 173, 293
York, D. G., Adelman, J., Anderson, J. E., Jr., et al. 2000, AJ, 120, 1579
Zabludoff, A. I., Zaritsky, D., Lin, H., et al. 1996, ApJ, 466, 104
Zhang, W., Li, C., Kauffmann, G., & Xiao, T. 2013, MNRAS, 429, 2191